Application of an integrated lumped parameter-CFD approach to evaluate the ejector-driven anode recirculation in a PEM fuel cell system

Giorgio Besagni *, Riccardo Mereu, Fabio Inzoli, Paolo Chiesa

Politecnico di Milano, Department of Energy, Via Lambruschini 4a, 20156 Milano, Italy

Proton exchange membrane fuel cells (PEMFCs) are considered a promising candidate to replace internal combustion engines. The unconsumed hydrogen, in PEMFC systems, is released at the anode exit and a recirculation can be applied to increase the fuel utilization; to this end, a recirculation system is needed and ejector technology is a promising technique, considering its many advantages. Unfortunately, ejectors are characterized by extremely complex fluid dynamic phenomena and a small deviation from the opti-mum operating condition might drastically lower the performances of the ejector itself and, consequently, of the whole ejector-based system. For this reason, multi-scale models—taking into account both the "*local-scale*" and the "*component-scale*" fluid dynamics phenomena—should be applied to evaluate the per-formance of ejector-based systems. In this paper, we contribute to the existing discussion concerning multi-scale modeling techniques and we propose an integrated lumped parameter- Computational Fluid Dynamics model to investigate the performance of convergent-nozzle ejectors for the anode recircu-lation in PEMFC systems. The integrated approach is based on a lumped parameter model (able to estimate the "*component-scale*" performance) with variable ejector component efficiencies, provided by Computational Fluid Dynamics simulations (able to predict the "*local-scale*" phenomena). Computational Fluid Dynamics simulations have been used to investigate the ejector "*local-scale*" fluid dynamic phenomena and to formulate correlations for ejector component efficiencies, thus linking ejector component efficiencies to the "*local-scale*" phenomena. In the first part of the paper, the integrated lumped parameter-Computational Fluid Dynamics approach has been formulated, validated and compared with different constant efficiency models, showing better performance and a wider range of applicability. In the second part of the paper, the integrated approach has been included in a complete PEMFC system model (considering both electro-chemical and pressure-drop effects). It has been demonstrate that a small deviation from the optimum operating condition of the ejector lower the performances of the whole system. The Integrated lumped parameter model-Computational Fluid Dynamics approach, because of the variable ejector component efficiencies, has been able to correctly consider the off-design performance of an ejector based system; conversely, constant ejector component efficiency models cannot correctly predict the performance of the PEMFC system. In conclusion, the use of variable ejector component effi-ciency models is needed in order to (a) provide a realistic model of the system and (b) analyze the performance in both for on- design and off-design performance. In addition, the proposed paper also provides a demonstration for the implementation of modeling involving both fluid dynamics and electro-chemical analysis in the context of fuel cells.

* Corresponding author at: Politecnico di Milano, Department of Energy, Via Lambruschini 4, 20156 Milan, Italy.
  E-mail addresses: giorgio.besagni@polimi.it (G. Besagni), riccardo.mereu@polimi.it (R. Mereu), fabio.inzoli@polimi.it (F. Inzoli), paolo.chiesa@polimi.it (P. Chiesa).

Nomenclature

1. Introduction

Proton Exchange Membrane Fuel Cell (PEMFC) technology is considered a promising candidate to replace internal combustion engines, considering its many advantages (i.e., high power density, high efficiency, rapid start-up and low emission). In this respect, the reader may refer to some recent review concerning PEMFC technologies for a more detailed discussion on the role of these systems (and the influence of their operating conditions and design criteria) as high-efficiency energy conversion systems (See, for example, Refs. [1–4]). In PEMFC energy conversion systems the fuel utilization factor is significantly lower than one in order to prevent severe voltage losses (due to a decrease of hydrogen concentration). Therefore, unconsumed hydrogen is released at the anode exit and a recirculation can be applied to increase the fuel utilization. Generally, mechanical pumps and compressors could be used, but they consume electrical power, generate vibrations, require lubrication, and need regular maintenance: these features are undesirable and, as consequence, a recirculation system based on ejector is a promising alternative.

Ejector is a device which provides a combined effect of (a) entrainment, (b) mixing, and (c) compression, with no-moving parts and without limitations concerning working fluids. An ejector is constituted by a primary nozzle, a suction chamber, a mixing zone, and a diffuser. A high-pressure primary flow entrains a secondary flow, they mix and a diffuser compresses the mixed stream (i.e., see the discussion proposed in Ref. [5]). The combined effects of entrainment, mixing, and compression as well as its many practical advantages (i.e., simplicity of construction, the lack of any mechanically operated parts, the reliability, the little maintenance, the low cost, and the long lifespan) are the characteristics making the ejector an interesting solution for many energy engineering systems (i.e., refrigeration technologies [5], high temperature energy conversions systems [6], and fuel cell systems—the subject of this paper). In particular, in PEMFC systems, the ejector employs the high-pressure hydrogen (the primary flow of the ejector) stored in a vessel to entrain the anodic exhaust (the secondary flow of the ejector) at the fuel cell stack anode inlet. The ejector design as well as its integration in a PEMFC system is proposed in Fig. 1a. It is worth noting that the primary nozzle can be either (a) conver-
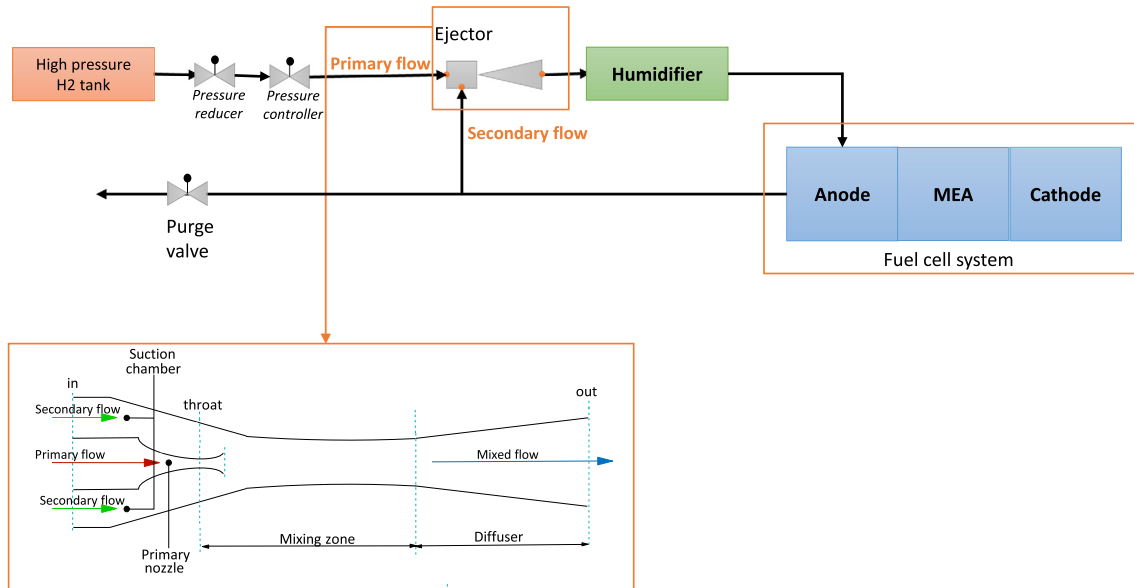
(a) Ejector-driven anode recirculation in a PEM fuel cell system
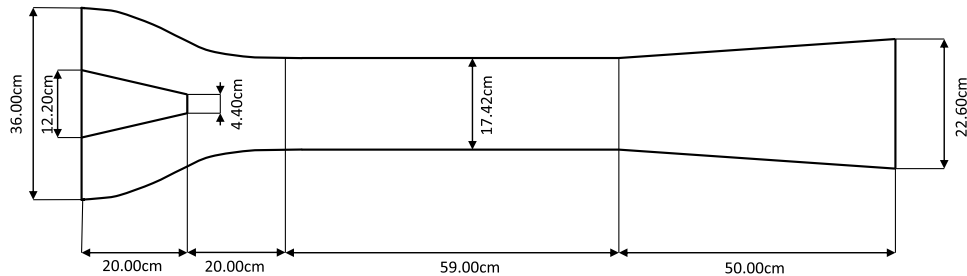
(b) Ejector design parameters in the proposed work

Fig. 1. PEMFC system layout and ejector design.

gent or (b) convergent-divergent, depending on the system application and requirements. In particular, in PEMFC technology, convergent-nozzle ejectors are used; such nozzle shape is used to avoid the "*flash boiling*" phenomenon (characterized by mechanical and thermal non-equilibrium effects), which implicates the condensation of water vapor entrained in the secondary flow, owing to owing to the low temperature of the primary and secondary flows. The interested reader may refer to the recent review pro-posed by Liao and Lucas for an overview concerning this topic [7]. Unfortunately, ejectors have a main drawback: they are characterized by extremely complex fluid dynamic phenomena and, as consequence of the fluid dynamics, a small deviation from the optimum operating condition might drastically lower the performances of the whole system (see Ref. [5] for an overview on this topic). For this reason, accurate models to predict both the on-design and the off-design ejector operating conditions are needed. To the authors' opinion, such accurate models should rely on a "*multi-scale*" approach, taking into account the fluid dynamics at the "*local-scale*" and at the "*component-scale*". The knowledge of the fluid dynamics at the "*local-scale*" concerns a correct prediction of the local fluid dynamic phenomena, i.e., boundary layers subject to adverse pressure gradients, shock waves, under-expanded jets, flow reparation, recirculation, turbulence mixing phenomena bounded by near-wall regions, ...); conversely, the knowledge of the fluid dynamics phenomena at the "*component-scale*" concerns a correct prediction of the entrainment ratio—defined as the ratio between the secondary and the primary mass flow rates—which measures the performance of the ejector. Of course, the behavior

at the "*component-scale*" is the result of the flow features inside the ejector at the "*local-scale*". Unfortunately, such "*multi-scale*" approach is usually not considered and, instead, lumped parameter and Computational Fluid Dynamics (CFD) models were mainly applied focusing on one of the two scales. In addition, lumped parameter and CFD models were mainly developed for convergent-divergent-nozzle ejectors (i.e., to be applied in refriger-ation systems) and only a limited number of models for convergent-nozzle ejectors are available, as summarized in the fol-lowing literature survey.

Kim et al. [8] proposed a design methodology for PEMFC ejector recirculation system in a submarine. He et al. [9] described a hybrid ejector-blower layout for PEMFC recirculation system. Bao et al. [10] proposed an analytical ejector model for PEMFC recircu-lation system, along with a control model. Zhu et al. [11] proposed a lumped parameter ejector model for PEMFC recirculation system, accounting for the local flow properties by using two-dimensional velocity profiles. Brunner et al. [12] presented and described the design and control modes of ejectors for PEMFC recirculation system using a two-dimensional ejector model. Maghsoodi et al.[13] proposed a two-dimensional ejector model and have numeri-cally investigated the optimum ejector design by artificial neural network and genetic algorithm approaches. Besagni et al. [14] pro-posed an integrated lumped parameter-CFD approach for off-design ejector performance evaluation. The proposed approach coupled a lumped parameter model to CFD simulations. In particular, the CFD simulations have been used to estimate the ejector component efficiencies applied in the lumped parameter model.

Indeed, the values of these efficiencies highly influence the accuracy of lumped parameter models and are generally taken as constant, even if their value depends on the working fluid, operating conditions, geometry and local fluid dynamic phenomena as demonstrated in different recent papers (See Refs. [14–19]). The reader should refer to the literature survey proposed in the introduction of Ref. [18] for a more detailed discussion concerning ejector component efficiencies. It is worth noting that ejector component efficiencies have high influence of performance of lumped parameter models have been demonstrated in our previous paper [20]. This paper contributes to the existing discussion and further develop our previous research [14]. In particular, the main goals of this study are as threefold:

1. to include a "*multi-scale*" model of the ejector within a full model of a PEMFC system, in order to model both the fluid dynamics and the electro-chemical phenomena in the context of fuel cells;
2. to use of variable ejector component efficiency formulations to provide a realistic model of the system (both the ejector component and the whole PEMFC systems);
3. to apply the integrated lumped parameter-CFD approach to study the on-design and off-design performances of ejector-based systems;

The present paper is structured as follows. In the first part, a lumped parameter model and a CFD model for a convergent-nozzle ejector have been presented and commented. The CFD approach has been used to investigate the ejector operating curves and to the influence of operating conditions over flow fields. Furthermore, the CFD approach has been used to (a) analyze ejector component efficiencies, (b) generate ejector component efficiency maps, (c) establish empirical equations for ejector component efficiencies and (d) investigates the relationship between ejector component efficiencies and local fluid dynamic phenomena (at different operating conditions). In addition, the influence of the working fluid has been studied and ejector component efficiency maps for the case of Hydrogen (which is used in the context of fuel cells) as the working fluid have been presented. In the second part, the Integrated lumped parameter model-Computational Fluid Dynamics approach has been formulated, it has been validated and compared with different constant ejector component efficiency models showing better performance and a wider range of applicability. In the third part, the model of the ejector has been included in a PEMFC fluid dynamics and electro-chemical model and the whole system has been simulated. Finally, the main conclusions and outcomes of this paper are drawn.

2. Computational fluid dynamics model

The CFD model described in the following of this section has been previously validated by the authors in our previous works (see Refs. [14,21]), to whom the reader should refer for further details on the numerical approach.

2.1. Ejector design

The following considerations were taken into account to design the convergent-nozzle ejector (Fig. 1b):

- the nozzle outlet position has been placed inside the suction chamber to achieve better performances (see, for example, Ref. [22]);
- the diameter of the mixing chamber, d_{mix} has been chosen considering $d_{mix}/d_t \approx 4$, which is in the range suggested by Alves [23] $d_{mix}/d_t = 3-6$;

- the length of the constant-area section, L_{mix}, has been chosen as a compromise between two effects. First, in a small mixing chamber the fully developed profile for the velocity might not occur, causing flow separation in the diffuser. Second, in a long mixing chamber, the pressure drop may be significant. In the present case $L_{mix}/d_t \approx 18$. The proposed value (higher than $L_{mix}/d_t = 10$, assumed by Marsano et al. [24]), has been chosen to provide a geometry suitable for the whole set of operating conditions analyzed;
- the conical shape diffuser has been design with 6° diverging angle [25].

Of course, the optimization of ejector geometry is a matter of ongoing studies.

2.2. Meshing approach

The mesh generations process has been handled with GAMBIT 2.4.6. A 2-dymensional axi-symmetric domain has been used to model the ejector, based on its symmetric nature. Quadrilateral elements have been used for minimizing the numerical diffusion. It is worth noting that numerical errors may depend on the mesh quality [26] and the criteria used in this study to limit them have been as follows: (a) maximum skewness below 0.5, (b) orthogonally higher than 0.75 and (b) maximum growth rate 20%. In addition, the mesh has been refined on the mixing layer and near-wall regions. The resulting grid has been initially made at about 40,000 quadrilateral elements and later adapted to about 320,000 elements to confirm that the results are grid independent. The grid independency considerations have been also based on the previous numerical results reported in Ref. [21], to whom the reader should refer. Furthermore, an adaptive meshing technique based on the gradient of the Mach number to refine the mesh has been used.

2.3. Solver, numerical settings and turbulence modeling

The fluid flow in the ejector is compressible and turbulent and, in the present case, it is considered as steady state. The relationship between density, velocity and temperature is given by the conservation of continuity, momentum, energy equations, in the form of a set of partial differential equations. In this paper, the finite volume commercial code ANSYS Fluent Release 14.0 has been used to solve the steady state 2D axisymmetric Reynolds Averaged Navier-Stokes (RANS) equations for the turbulent compressible Newtonian fluid flow.

The governing equations have been discretized as follows. High order schemes (the MUSCL scheme schemes) have been used for the spatial discretization, in order to limit the numerical diffusion. Second order schemes have been used also for the turbulence quantities. Gradients have been evaluated by a least-squares approach. After the discretization process of the governing equations, a system of algebraic equations has been obtained and it has been solved: due to the strong coupling between mass, momentum and energy equations, determined by the presence of a high speed compressible flow, a density-based coupled solver has been chosen and applied. In ANSYS Fluent, both density-based and pressure-based algorithms are available: a comparative discussion concerning density-based and pressure-based algo-rithms to solve ejector fluid dynamics was provided by Croquer et al. [27]. The Coupled algorithm applied solves the continuity, momentum, and energy (density has been computed through the equation of state selected (See Section 3.2.3)) equations simultane-ously. The formulation of the coupled algorithm requires setting up a Courant–Friedrichs–Lewy (CFL) condition; it has been set CFL = 1 in order to run a stable simulation (the *CFL* = 1 condition is based on sensitivity analysis, based on both convergence capability and

result quality). This value is suggested for future studied). Indeed, even if a steady case is investigated, the time marching is assumed to proceed until a time-invariant solution has been obtained (time discretization has been instead treated by using an Euler implicit scheme). Because of the complex fluid dynamics and in order to achieve fast convergence, a full multi-grid (FMG) initialization scheme has been adopted. Similar numerical approach has been formulated and applied in our previous papers [14,21] and is suggested to be applied in ejector simulations.

The turbulent behavior has been treated using the Reynolds averaging principle (RANS). The Reynolds averaged approach requires Reynolds stress components and Reynolds-average scalar transport equation extra terms to be modeled in an appropriate way. In our previous studies (see Refs. [14,21]) the most widely used RANS turbulence models have been compared and evaluated for both convergent-nozzle [14] and convergent-divergent-nozzle [21] ejectors: Spalart-Allmaras, k-ε Standard, k-ε RNG, k-ε Realizable, k-ω Standard, k-ω SST and linear RSM (Reynolds-Stress-Model). As a result, the k-ω SST showed the best performance for the different operating conditions and geometry studied and has been selected in this study. The interested reader should refer to our previous paper for the detailed analysis. Moreover, also in previous literature studied, the k-ω SST was proved to achieve good results concerning the shock wave prediction [28,29], the mean line of pressure recovery [28], the boundary layer separation [29] and the prediction of the vortex region downstream nozzle [30]. Finally the k-ω SST showed better performance, if compared to other RANS models, in modeling the fluid dynamics of ejectors, nozzles and diffuser flows [31,32].

2.4. Boundary conditions

Pressure-based boundary conditions (in the ANSYS FLUENT implementation) have been applied to the two inlets and to the outlet section (as displayed in Fig. 1a) and they have been chosen in order to analyze the possible flow behaviors in a convergent-nozzle ejector. In order to ensure a stable solution, the value of the pressure-outlet boundary condition has been discretely increased until convergence during the initialization process. The boundary conditions at the walls have been set as adiabatic and no-slip. For each value of the primary flow pressure, we increased the outlet pressure from very low values to higher values, till the occurrence of the back-flow conditions.

The turbulence intensity and hydraulic diameter have been chosen as turbulence boundary conditions; unfortunately, no turbulence measurements have been performed and the same approach as the one described in our previous paper [14] has been applied: (i) the turbulence viscosity ratio ($\mu_t/\mu = 500$ and $\mu_t/\mu = 100$, for the primary and the secondary flow, respectively) and (ii) a turbulence intensity ($I = 5\%$ for and $I = 2\%$, for the primary and the secondary flow, respectively). These values are based on the work proposed by Georgidias and Debonis [33], who studied the influence on the turbulence boundary conditions for a convergent-nozzle ejector. Future studies will be devoted to study the effects of uncertainties on turbulence boundary conditions on the prediction of the numerical model (See, for example, Ref. [34]).

2.5. Working fluids

The working fluid has been modeled as ideal gas and the properties (thermal conductivity, specific heat capacity and viscosity) of the air at atmospheric pressure and temperature of 25 °C have been used. The modeling as ideal gas has been mainly based on the working fluid and the operating conditions adopted in the cases analyzed here. Furthermore, in the literature several studies adopt this approach in CFD analysis, as discussed in our previous paper [14].

2.6. Convergence criteria

The numerical solution has been considered as converged when all the following converging criteria have been satisfied simultaneously: (a) a decrease in numerical residuals by six orders of magnitude; (b) the normalized difference of mass flow rates at the inlet and at the outlet passing through the modeled ejector has to be less than 10^{-7}; (c) the area-weighed-averaged value for inlet velocity of primary and secondary flow is constant. The interested reader should refer to the discussion concerning physical and numerical convergence in Refs. [14,21].

3. Lumped parameter model (LPM) for ejector performance evaluation

A steady-state lumped parameter model (LPM) for a convergent-nozzle ejector performance evaluation has been developed. The proposed model can be integrated with the ejector component efficiency maps, thus creating the ILPM-CFD model.

3.1. On-design and Off-design operation conditions

Before presenting the LPM, some details are given, in the following, concerning the ejector operation modes. A convergent-nozzle ejector works, depending on its boundary conditions, in three operating modes:

o **the critical mode.** The primary flow is choked; the secondary mass flow rate is constant;
o **the subcritical mode.** The primary flow is not choked; the secondary mass flow rate depends on the value of the exit pressure;
o **malfunction mode (back-flow).** The primary flow reverses in the suction chamber.

It is worth noting that these operating modes physically manifest in the ejector operating curves, as the ones presented in Ref. [5]. In this paper, we refer to on-design operation when the ejector works in the critical mode and the primary flow is chocked. Conversely, when the primary flow is not chocked we refer to off-design operation. The ejector may work in the off-design operating conditions during the changes of load or during the start-ups. Thus, the correct evaluation of both on-design and off-design operating conditions are very important in the modeling of the whole ejector-based system. In order to take into account the off-design operating conditions, two conditions should be satisfied: (a) the mathematical formulation of the LPM should be suitable; (b) variable ejector component efficiencies should be used to take into account the local fluid dynamic phenomena. Indeed, the appropriate mathematical structure of the LPM is not enough to ensure the correct modeling of the off-design condition and the ILPM-CFD model is needed (by using variable component efficiencies).

3.2. LPM assumptions

The following assumptions have been made, when developing the lumped parameter model:

1. ejector walls have been considered as adiabatic (isentropic efficiency can be applied to account for non-ideal processes);
2. primary and the secondary fluids have been considered as ideal gases;
3. velocity and thermodynamic properties have been considered as uniformly distributed in each cross-section;
4. primary and secondary flows have total conditions at inlets.

The above-listed assumptions are common to the LPMs found in the literature. The reader should refer to the review of He et al.[22], concerning the mathematical models till 2009, and to the paper of Besagni et al. [20], concerning the comparison of five dif-ferent LPMs. The above-mentioned assumptions are, therefore, coherent with the typical assumptions made while developing LPMs. It is important to notice that, in the perspective coupling the LPM and the CFD approach, the same thermodynamic proper-ties should be used (i.e., the hypothesis of ideal gas).

The proposed lumped parameter mode provides as output the entrainment ratio $\omega = \dot{m}_s/\dot{m}_p$, by using as input (a) the ejector geometry, (b) $p_{p,in}$, (c) $p_{s,in}$, (d) $T_{p,in}$, and (e) $T_{s,in}$. One additional information is needed to close the mathematical formulations of the problem. In the present paper the primary mass flow rate, $\dot{m}_s$, has been used. Instead of $\dot{m}_s$, other parameters to close the mathematical formulations of the problem can be (a) the pressure at the outlet (p_{out}), (b) a hypothesis on the velocity distribution inside the ejector or (c) the Mach number at suction nozzle outlet ($M_{s,t}$).

3.3. LPM model structure

The LPM has been structured to solve firstly (a) the suction chamber, secondly (b) the primary nozzle, thirdly (c) the mixing chamber and, finally, (d) the diffuser. It is worth noting that the proposed LPM differs from the models presented in the literature for the solving procedure itself (the reader should refer, for exam-ple, to the model of Huang et al. [35] or the model of Zhu et al. [36], to the model comparison of Besagni et al. [20] and to the review of He et al. [22]). The main difference from the previous model pro-posed in the literature is that, in the present case, the first ejector component to be solved is the suction chamber and not the pri-mary nozzle.

3.3.1. Suction chamber

Given as input parameters (a) the secondary mass flow rate ($\dot{m}_s$) and (b) the inlet conditions of the secondary flow ($T_{s,in}$ and $p_{s,in}$), the Mach number of the secondary flow at the suction chamber exit ($M_{s,t}$) is computed as follows:

$$M_{s,t} = \frac{\dot{m}_s}{p_{s,in}A_{s,t}\sqrt{\frac{\gamma\eta_s}{R^*T_{s,in}}\left(1 + \frac{\gamma-1}{2}M_{s,t}^2\right)^{\frac{\gamma-1}{\gamma+1}}}} \tag{1}$$

where $A_{s,t}$ is the area at the exit of the suction chamber and η_s is the isentropic efficiency, which takes into account the friction losses and the irreversibilities. In particular, η_s is the ratio between the static enthalpy drop across the suction chamber and the isentropic drop from the same initial conditions to the final static pressure, defined as follows:

$$\eta_s = \frac{h_{s,in} - h_{s,t}}{h_{s,in} - h_{s,t,is}} \tag{2}$$

Hence, static temperature, pressure and velocity at suction chamber exit have been computed as follows (Eqs. (3)(5)):

$$T_{s,t} = \frac{T_{s,in}}{1 + \frac{\gamma-1}{2}\eta_s M_{s,t}^2} \tag{3}$$

$$p_{s,t} = \frac{p_{s,in}}{\left(1 + \frac{\gamma-1}{2}\eta_s M_{s,t}^2\right)^{\frac{\gamma}{\gamma-1}}} \tag{4}$$

$$v_{s,out} = \frac{\dot{m}_s}{\rho_{s,t}A_{s,t}} = R^*T_{s,t}\frac{\dot{m}_s}{p_{s,t}A_{s,t}} \tag{5}$$

3.3.2. Primary nozzle

In a convergent-nozzle ejectors, the primary flow can be either subsonic or chocked/sonic. The flow is subsonic when the pressure ratio (between the nozzle throat and the inlet) is lower than:

$$v_{cr} = \left(\frac{p_{s,t}}{p_{p,in}}\right)_{cr} = \left(\frac{2}{\gamma+1}\right)^{\frac{\gamma}{\gamma-1}} \tag{6}$$

If the primary flow is not chocked, $p_{p,t}$ is equal to $p_{s,t}$, otherwise it is not influenced by secondary flow. In the following, the primary noz-zle isentropic efficiency, η_p, is used to account for the friction losses and irreversibilitis:

$$\eta_p = \frac{h_{p,in} - h_{p,t}}{h_{p,in} - h_{p,t,is}} \tag{7}$$

In the case of chocked primary flow ($p_{p,in} \geq p_{s,t}/v_{cr}$), $M_{p,t}$, $p_{p,t}$ and $\dot{m}_s$ have been obtained from isentropic relations as follows:

$$\dot{m}_p = p_{p,in}A_{p,t}\sqrt{\frac{\eta_p\gamma}{R^*T_{p,in}}\left(\frac{2}{\gamma+1}\right)^{\frac{\gamma+1}{\gamma-1}}} \tag{8}$$

$$M_{p,t} = 1 \tag{9}$$

$$p_{p,t} = \frac{p_{p,in}}{\left(1 + \frac{\gamma-1}{2}\eta_p M_{p,t}^2\right)^{\frac{\gamma}{\gamma-1}}} \tag{10}$$

In the case of non-chocked (sub-sonic) primary flow ($p_{p,in} < p_{s,t}/v_{cr}$)), $M_{p,t}$, $p_{p,t}$ and $\dot{m}_s$ have been obtained from isentropic relations as follows:

$$\dot{m}_p = A_{p,t}p_{p,in}\sqrt{\frac{2\eta_p\gamma\left[\left(\frac{p_{s,t}}{p_{p,in}}\right)^{\frac{2}{\gamma}} - \left(\frac{p_{s,t}}{p_{p,in}}\right)^{\frac{1+\gamma}{\gamma}}\right]}{R^*T_{p,in}(\gamma-1)}} \tag{11}$$

$$M_{p,t} = \sqrt{2\frac{\left[1 - \left(\frac{p_{s,t}}{p_{p,in}}\right)^{\frac{\gamma-1}{\gamma}}\right]}{(\gamma-1)}} \tag{12}$$

$$p_{p,t} = p_{s,t} \tag{13}$$

3.3.3. Mixing zone

The evaluation of the mixing process is simpler than constant pressure or constant area models: in the proposed approach the hypothesis of aerodynamic throat or premixing zone is not used. Conversely, the behavior of the ejector has been described by ejec-tor component efficiency maps introduced in the balance equa-tions. The balance equations have been written by considering the control volume between the nozzle throat plane and the mix-ing zone outlet. The balance equations are as follows:

• momentum balance equation:

$$\eta_{mix}[(\dot{m}_p v_{p,t} + p_{p,t}A_{p,t}) + (\dot{m}_s v_{s,t} + p_{s,t}A_{s,t})]$$
$$= (\dot{m}_s + \dot{m}_p)v_{mix} + p_{mix}A_{mix} \tag{14}$$

• energy balance equation:

$$\dot{m}_p \left(c_{p,p} T_{p,t} + \frac{v_{p,t}^2}{2} \right) + \dot{m}_s \left(c_{p,s} T_{s,t} + \frac{v_{s,t}^2}{2} \right)$$

$$= (m_s + m_p) \left(c_{p,mix} T_{mix} + \frac{v_{mix}^2}{2} \right) \qquad (15)$$

• mass balance equation:

$$\dot{m}_p + \dot{m}_s = \frac{p_{mix} v_{mix} A_{mix}}{R^* T_{mix}} \qquad (16)$$

Solving Eqs. (15)(17) together, the mixing zone parameters p_{mix}, T_{mix} and v_{mix} have been obtained. The mixing efficiency η_{mix} has been defined from the above equations as follows:

$$\eta_{mix} = \frac{(\dot{m}_s + \dot{m}_p) v_{mix} + p_{mix} A_{mix}}{(\dot{m}_p v_{p,t} + p_{p,t} A_{p,t}) + (\dot{m}_s v_{s,t} + p_{s,t} A_{s,t})} \qquad (17)$$

3.3.4. Diffuser

The diffuser has been evaluated, by the following equation:

$$p_{out} = p_{mix} \left(\eta_d \frac{\gamma - 1}{2} M_{mix}^2 + 1 \right)^{\frac{\gamma}{\gamma - 1}} \qquad (18)$$

where η_d is the diffuser isentropic efficiency, which takes into account the friction losses and the irreversibility as follows:

$$\eta_p = \frac{h_{d,mix} - h_{d,out}}{h_{d,mix} - h_{d,out,is}} \qquad (19)$$

3.4. LPM solving procedure

Starting from $p_{p,in}$, $p_{s,in}$, $T_{p,in}$, $T_{s,in}$ and $\dot{m}_s$, the suction chamber has been solved (Eqs. (1), (3)(5)). Subsequently, the flow condition through primary nozzle has been evaluated (Eq. (6)) and primary nozzle has been solved by using equations for the case of (a) chocked flow (Eqs. (8)(10)) or (b) subsonic flow (Eqs. (11)(13)). Finally, the mixing zone and the diffuser have been solved (Eqs.(15)(18)) and the ejector outlet conditions have been obtained.

4. CFD results and ejector component efficiency evaluation

In this section, first, the CFD results have been presented and, second, the ejector flow efficiency maps have been obtained. Before presenting and discussing the numerical results it is worth noting that the flow fields in convergent-nozzle ejector flow fields are as follows: (a) back-flow flow field, (a) subsonic flow field, (c) moderately under-expanded and (d) highly under-expanded jet, as deeply discussed (and referenced) in our previous paper [14]. The discussion is not repeated here.

4.1. Ejector performance and flow phenomena

4.1.1. Fluid dynamics at the "component-scale": Ejector operating curves

Fig. 2 displays the operating curves obtained: the ejector operating curves describe, for a given primary flow pressure, the relationship between the outlet pressure (p_e) and the secondary mass flow rate ($\dot{m}_s$). It is worth noting that the operating curves (the relation between $p_e - \dot{m}_s$, for given primary pressure, $p_{0,p}$) describe and summarize all the information concerning the ejector fluid dynamics. Indeed, depending on the primary flow pressure (and for fixed ejector design), the entrainment effect is mainly related to the outlet pressure. In this perspective, the shape of

the operating curves reflects and summarizes all the complexity of the ejector fluid dynamics, from the "*local-scale*" (i.e., boundary layers subject to adverse pressure gradients, shock waves, under-expanded jets, flow reparation, recirculation, turbulence mixing phenomena bounded by near-wall regions,...) to the "*component-scale*" (i.e., entrainment effect, ...). A complete discussion of the operating curves for convergent-nozzle ejector has been proposed in Ref. [5], to whom the reader should refer. In the present case, the critical discharged pressure—corresponding to $\dot{m}_s = 0$, the onset of the back flow condition—increases while increasing the primary flow pressure. The secondary mass flow rate increases while increasing the primary flow pressure for a fixed discharged pressure. The former observation is in agreement with the previous literature. Conversely, the latter observation differ from what is observed in convergent-divergent nozzle ejector and is related to the fluid dynamic phenomena in convergent-nozzle ejector and the over-expansion of the jet at primary nozzle outlet, thus provid-ing larger entrainment effects. It has been observed that the sec-ondary flow does not reach the chocking condition. This occurs for two reasons: (a) the mixing chamber diameter is larger if com-pared to common ejectors [22] and, thus, the aero-dynamic throat is larger; (b) in a convergent-nozzle ejector has less entrainment effect compared to a convergent-divergent-nozzle ejector. Indeed, primary flow may reach only sonic condition at nozzle outlet and the primary flow cannot accelerate the secondary flow effectively like in a convergent-divergent-nozzle ejector (a similar observa-tion was made in Ref. [36]).

4.1.2. Fluid dynamics at the "local-scale": Effects of pressure boundary conditions on the local flow phenomena

The influence of the primary flow pressure and outlet pressure have bene presented in Fig. 3a and Fig. 3b respectively. Conversely, Fig. 4 displays the relationship between axial position in the ejec-tor and the shear stress at wall, to better describe the local flow phenomena and, in particular, the flow separation and recirculation.

The influence of the primary flow pressure $p_{0,p}$ has been dis-played in Fig. 3a (case#a to case#e) and has been presented in the following in terms of the Nozzle Pressure Ratio (NPR), defined as the ratio between primary and secondary inlet pressure (NPR = $p_{0,p}/p_{0,s}$). At NPR = 1.5 the flow field is subsonic and the noz-zle is not chocked (Fig. 3a, case#a); the primary flow core is short and mixing process is completed before entering the diffuser; in additions, flow separation occurs in the mixing chamber (Fig. 4). In particular, Fig. 4 displays the relationship between axial position in the ejector and the shear stress at wall: a zero value of shear stress at wall indicates flow separation and recirculation phenom-ena. At NPR = 3, a moderately under-expanded jet is observed and the nozzle is chocked (Fig. 3a, case#a); the over-expansion of the jet causes a shock-diamond structure; the flow separation occurs at the diffuser inlet, as visualized in Fig. 4. At NPR = 5, under-expanded jet is present (Fig. 3a, case#c). The supersonic structure is characterized by stronger shock-waves. The primary jet core length occupies almost the whole mixing chamber's length. At NPR = 7.5, highly under-expanded jet is present (Fig. 3a, case#d). The structure of the primary jet core influences secondary flow: the continuous change in the available section for the secondary flow causes a series of expansion and compression. At NPR = 10 (Fig. 3a, case#e), a highly under-expanded jet is observed and a Mach dish appears at the nozzle exit (Fig. 3a, case#e). Secondary flow is almost chocked. The influence of the outlet pressure (for the fixed inlet conditions of Fig. 3a, case#b), is displayed in Fig. 3 (right): starting from low value, p_e is increased till the back-flow condition. Increasing p_e, ejector changes operating condition from critical (Fig. 3a, case#a), where secondary flow almost chocked,
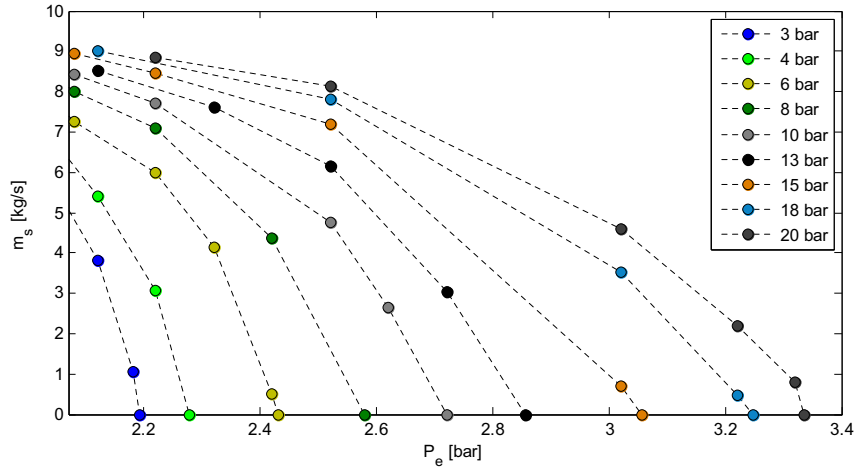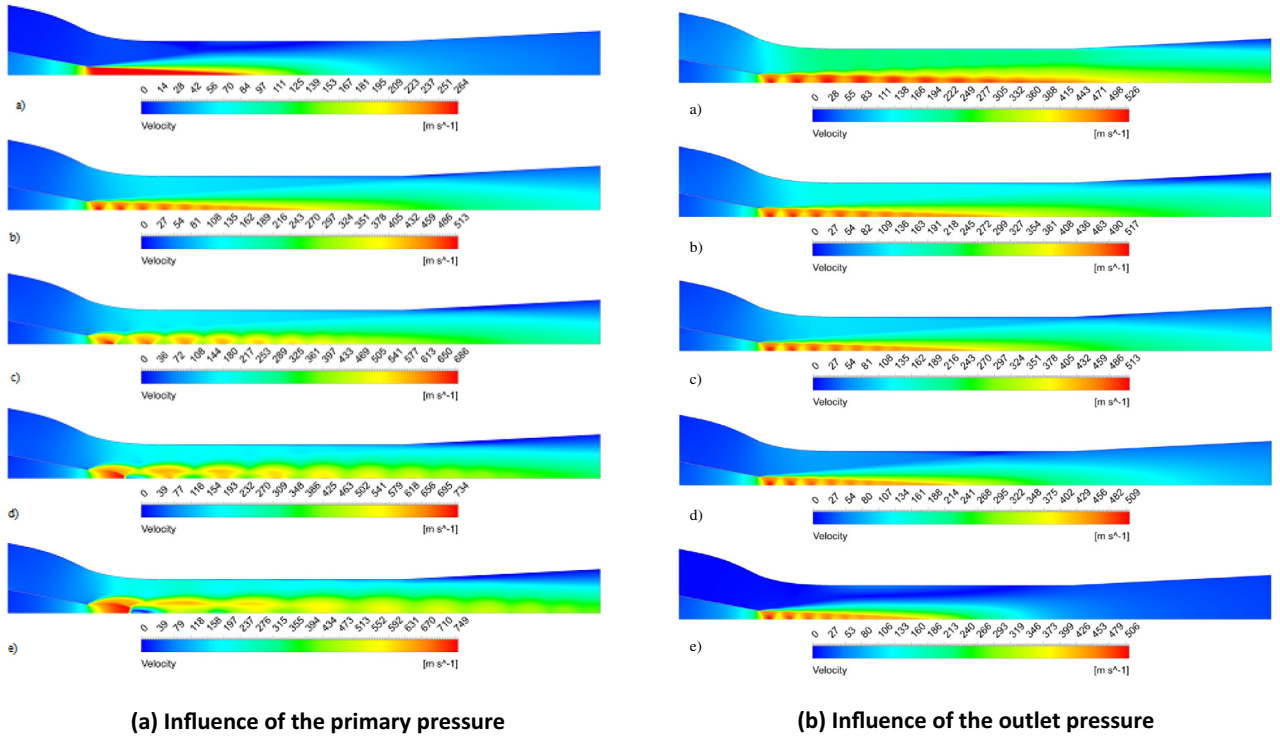
Fig. 2. CFD results: ejector operating curves.

(a) Influence of the primary pressure

(b) Influence of the outlet pressure

Fig. 3. CFD results – Fig. 3a: Influence of primary pressure: (a) 3 bar, (b) 6 bar, (c) 10 bar, (d) 15 bar, (e) 20 bar – p^e = 2.22 bar; Fig. 3b: Influence of the outlet pressure: (a) 1,88 bar, (b) 2,08 bar, (c) 2,22 bar, (d) 2,32 bar, (e) 2,42 bar.

to subcritical (Fig. 3b, case#b). The increase of p_e causes two effects: (i) the decrease of the primary jet-core length (primary fluid encounters an adverse pressure gradient) and (ii) the decrease of the maximum secondary flow velocity.

4.2. Ejector component efficiencies

The information on every flow field, obtained by using the CFD model, has been used to evaluate ejector component efficiencies. In particular, the primary nozzle efficiency, the suction chamber efficiency, the mixing zone efficiency and the diffuser efficiency have been computed by using the iterative process proposed and described by Maddiotto [37], which has been derived from the method proposed by Liu and Groll [16]. The input data, to compute the ejector component efficiencies, have been computed as mass

averaged quantities except for pressure, in which case area averaging has been applied. Thermodynamic properties have been evaluated by using FluidProp [38] and TPSI as the thermodynamic library. An analysis showed that the ejector component efficiencies can be expressed as a function of two parameters:

- nozzle pressure ratio (NPR), defined as follows:

$$NPR = p_{0,p}/p_{0,s} \tag{20}$$

- dimensionless secondary mass flow rate ($\dot{m}_{s,ad}$), defined as follows:

$$\dot{m}_{s,ad} = m_s \sqrt{R^* T_s}/p_{0,s} A_{s,out} \tag{21}$$

In the following paragraphs, regression functions for ejector component efficiencies have been proposed. Those empirical correlations
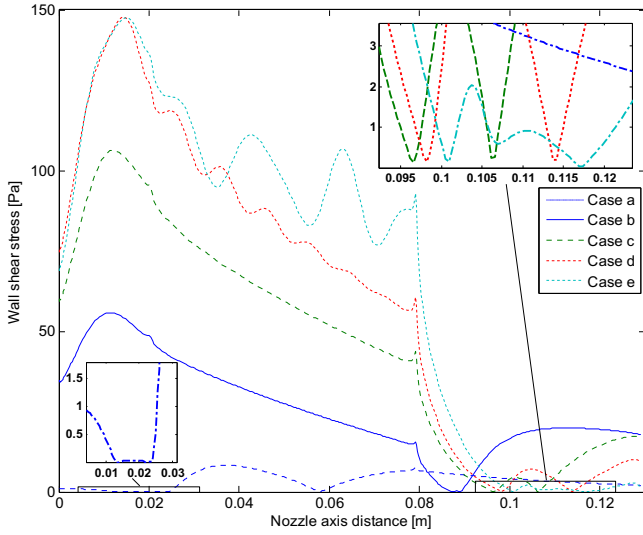
Fig. 4. Influence of the primary pressure on the flow separation (Code to Fig. 3a).

have been obtained, and should be used, within the following boundaries:

$$1.43 < NPR < 9.51 \tag{22}$$

$$0.017 < \dot{m}_{s,ad} < 0.356 \tag{23}$$

In the next section, our results have been compared with previous studies proposed in the literature concerning ejector component efficiencies (i.e., Refs. [14–16,18,19]). A qualitative comparison has been performed. However, it is worth noting that a come detailed comparison is hardly possible because of differences in ejector geometry, refrigerant used, the presence of multiple phases and, eventually, metastable effects.

4.2.1. Primary nozzle

The primary nozzle efficiency, η_p, mostly depends on *NPR* (Fig. 5). η_p ranges from low values ($\eta_p = 0.88$, subsonic flow field) to an asymptotic higher value ($\eta_p = 0.975$, highly under-expanded jet). The asymptotic value is caused by the presence of the super-

sonic structure appearing at the nozzle exit and preventing downstream information to travel upstream. In this condition, η_p does not depend anymore from nozzle exit conditions, resulting in a constant value. These results are in agreement with the results and the considerations provided by Besagni et al. [14]. In a previ-ous investigation, Varga et al. [15] (single phase ejector – R718) reported η_p independent from outlet conditions (the motive nozzle was chocked). In addition, the range of η_p found by Liu and Groll [16] (considering a two-phase ejector – R744) agrees with our results. More recently, Wang and Yu [19] (considering a two-phase ejector – R600) proposed valued and trends of the motive nozzle efficiency quite different from the proposed ones (the motive nozzle efficiency decreases while increasing the *NPR*): these results can be caused by metastable effects in two-phase ejectors and the different working fluid employed, as well as the different geometry. Zheng and Deng [18] (two-phase ejector – R744) found that the primary nozzle efficiency first decreases and then increases with the increase in NPR. In particular, the values of the motive nozzle efficiency obtained at high NPR agrees with our results.

4.2.2. Suction chamber

Suction chamber efficiency mostly depends upon $m_{s,ad}$. (Fig. 6). When the secondary mass-flow rate is high, η_s reaches its maximum value ($\eta_s = 0.88$, highly under expanded jet). When back-flow conditions have been reached η_s drops, due to a flow separa-tion near the nozzle exit. This causes reverse flow in the suction chamber, which is correctly predicted by the low value of η_s. The shape of the suction chamber in the previous studies is quite differ-ent and the results of Varga et al. [15] (η_s is nearly constant in crit-ical condition and drops in subcritical operation) confirm our results for the constant value of η_p. This trend was also observed by Liu and Groll [16] and by Zheng and Deng [18].

4.2.3. Mixing zone

Mixing zone efficiency depends on both *NPR* and $m_{s,ad}$ (Fig. 7). η_{mix} ranges between $\eta_{mix} = 60\%$ (subsonic flow field) and $\eta_{mix} = 74\%$ (under expanded jet). η_{mix} increases with the primary pressure and decreasing the discharged pressure. The decrease of the mixing chamber efficiency with the increase of the back pressure is due to an adverse pressure gradient, causing: (a) reduction of the pri-
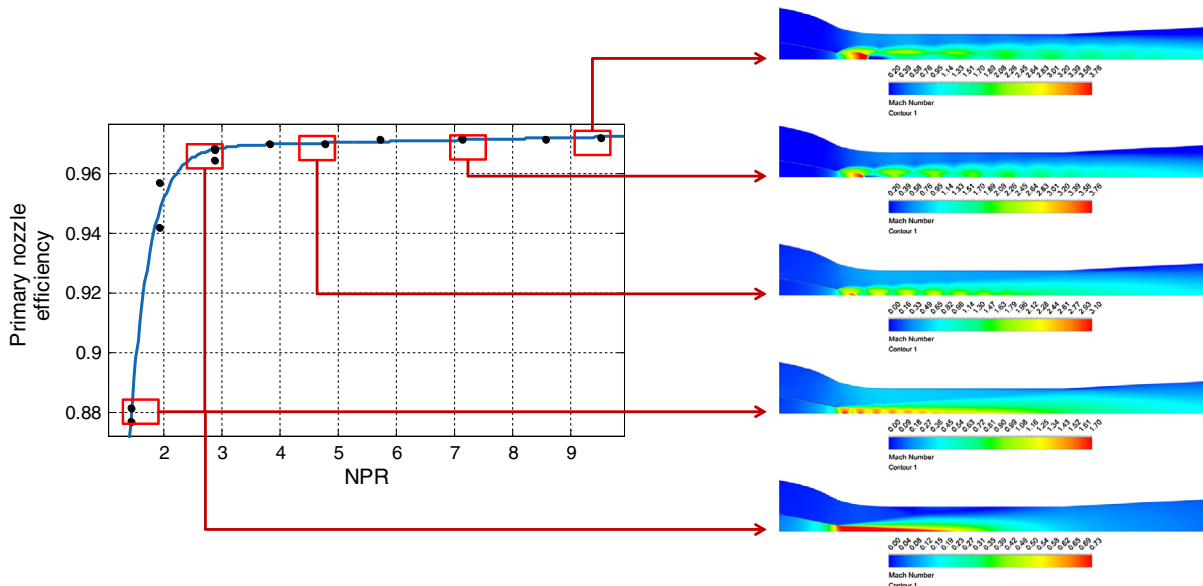

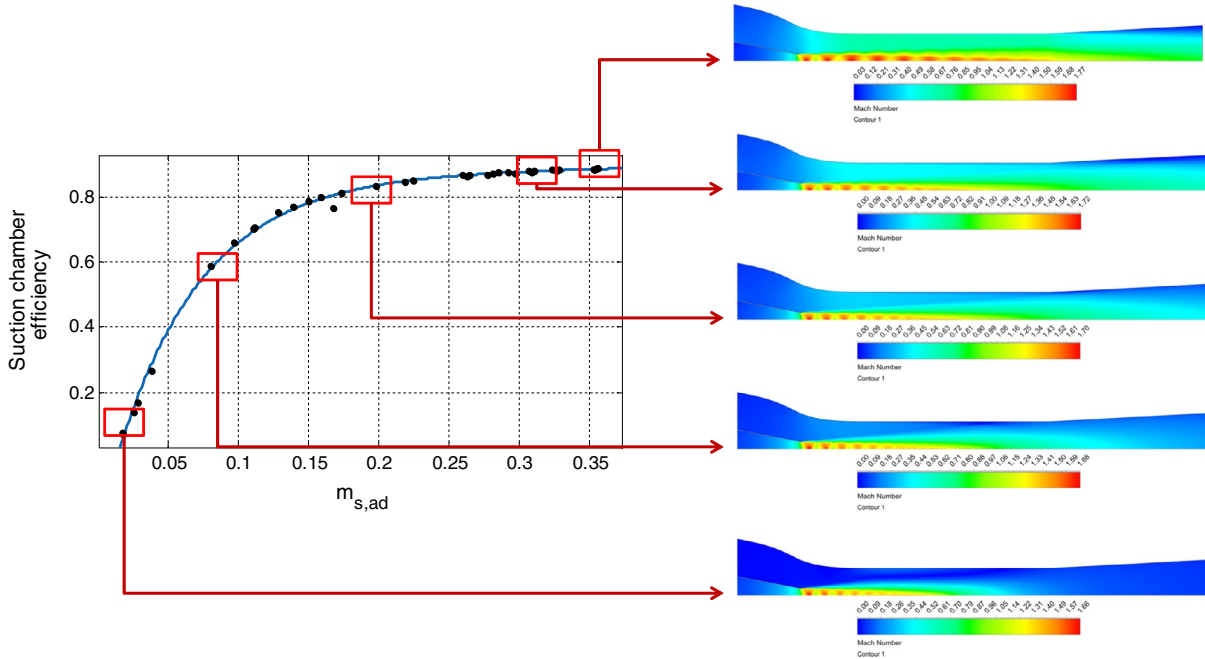**Fig. 5.** Primary nozzle: relations between efficiencies and flow phenomena.

Fig. 6. Suction chamber: relations between efficiencies and flow phenomena.

mary flow jet-core and (b) a flow separation zone near the wall. This effect is more relevant for low primary pressures. For higher pressures this is less important because primary mass flow rate is higher and the primary flow jet core is not influenced by the separation zone. At last, η_{mix} decreases near the back flow condition. The range of variation of η_{mix} in our study is similar to the one by Varga et al. [15], Liu and Groll [16], Besgani et al. [14] and Wang and Yu [19].

4.2.4. Diffuser

Diffuser efficiency depends on both *NPR*, and $m_{s,ad}$ (Fig. 8). η_d increases while increasing the back-pressure and decreasing the primary flow pressure. The behavior of the diffuser is the opposite of the mixing chamber. Indeed, for low p_e values, the velocity in the entrance of the diffuser is high, resulting in a flow separation zone near the wall. When the primary pressure is higher the velocity of the primary jet core is higher, leading to flow separation with an efficiency drop. Finally, η_{dif} increases with p_e (ranging from 0.5 to 0.85): at low p_e, the final shock wave is observed inside the diffuser (Fig. 3, right). At higher back-pressure, the shock wave moves back into the mixing zone, and the flow in the diffuser is subsonic, decreasing the losses.

4.2.5. Ejector component efficiency maps

Ejector component efficiency maps have been obtained by using regression equations (Table 1). It should not escape that regression equations have uncertainty associated to their parameters. Those equations have been chosen as the best compromise between complexity and good approximation of CFD data. Four regression functions have been obtained: two exponential regression functions for the primary nozzle and the suction chamber, and two polynomial functions for the mixing chamber and the diffuser. The ejector component efficiency maps have been displayed in Fig. 9.

4.2.6. Influence of the working fluids

The change of working fluid leads to a change in fluid properties (i.e. molecular mass, viscosity and density) and a change in the Reynolds number, the sonic velocity and the friction losses. The ejector component efficiency maps presented in Section 4.2.6 can

be used for different working fluids if the similitude is respected. The detailed explanation of the similitude analysis for the case of an ejector was presented by Brunner et al. [12]. Given the non-dimensional analysis and the flow fields investigated, in the pre-sent case the similitude is ensured under the following conditions:(a) equality of *Re*, (b) equality of Mach number, (c) equality of γ and (d) geometrical similitude. Under the hypothesis of ideal gas, the equality of γ means that these maps are valid for diatomic gases. The influence of the working fluid is better presented for the case of Hydrogen: 18 additional simulations have been performed using Hydrogen as working fluid and considering the operating range analyzed of a PEMFC systems (see Ref. [36]). Hydrogen ejector component efficiency regressing equations have been presented in Table 2. Primary nozzle and suction chamber have the same behavior comparing hydrogen and air (Fig. 10a, b). Conversely, lit-tle differences have been observed for the mixing chamber and the diffuser; however, the qualitative trend is the same (Fig. 10c, d).

5. Integrated LPM-CFD model for ejector performance evaluation

5.1. Coupling between LPM and CFD models

The integrated LPM-CFD approach is based on a lumped parameter model (able to predict the "*component-scale*" performance – Section 3) with variable ejector component efficiencies, provided by Computational Fluid Dynamics simulations (able to predict the "*local-scale*" – Sections 2 and 4). In particular, the CFD (Sections 2 and 4) and the LPM (Section 3) approaches have been coupled by using the ejector component efficiency maps obtained in Sec-tion 4.2.5. The ejector component efficiencies account for the local fluid dynamic phenomena in the lumped parameter model. In this respect, the influence of the number of points to build the effi-ciency maps of the ejector on the ILPM-CFD model has been inves-tigated and the results have been presented in Appendix A. It is worth noting that the ejector component efficiency maps can be applied in the LPM because (a) the definitions of the efficiencies are the same in the CFD and the LPM approaches; (b) the CFD
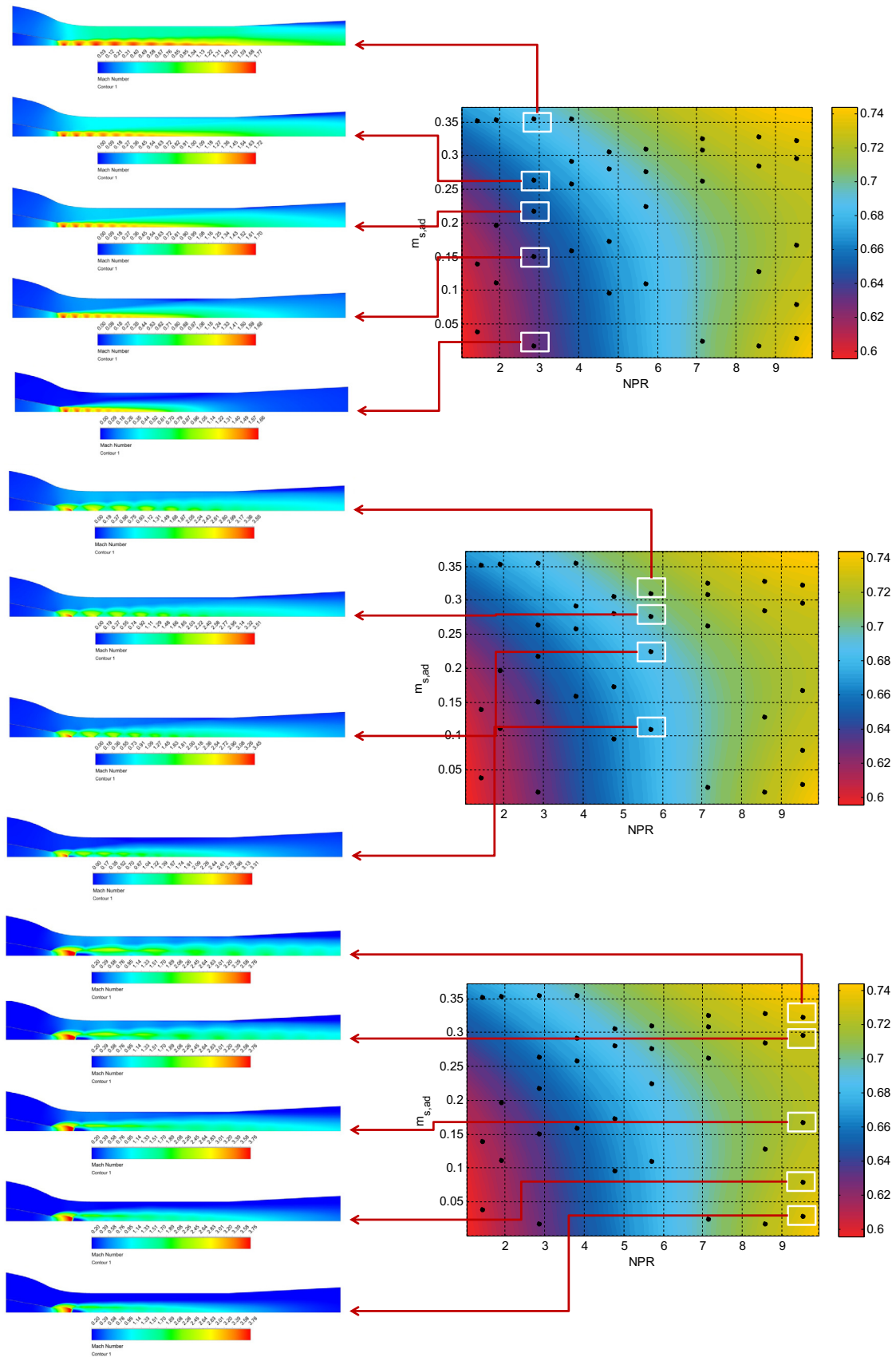
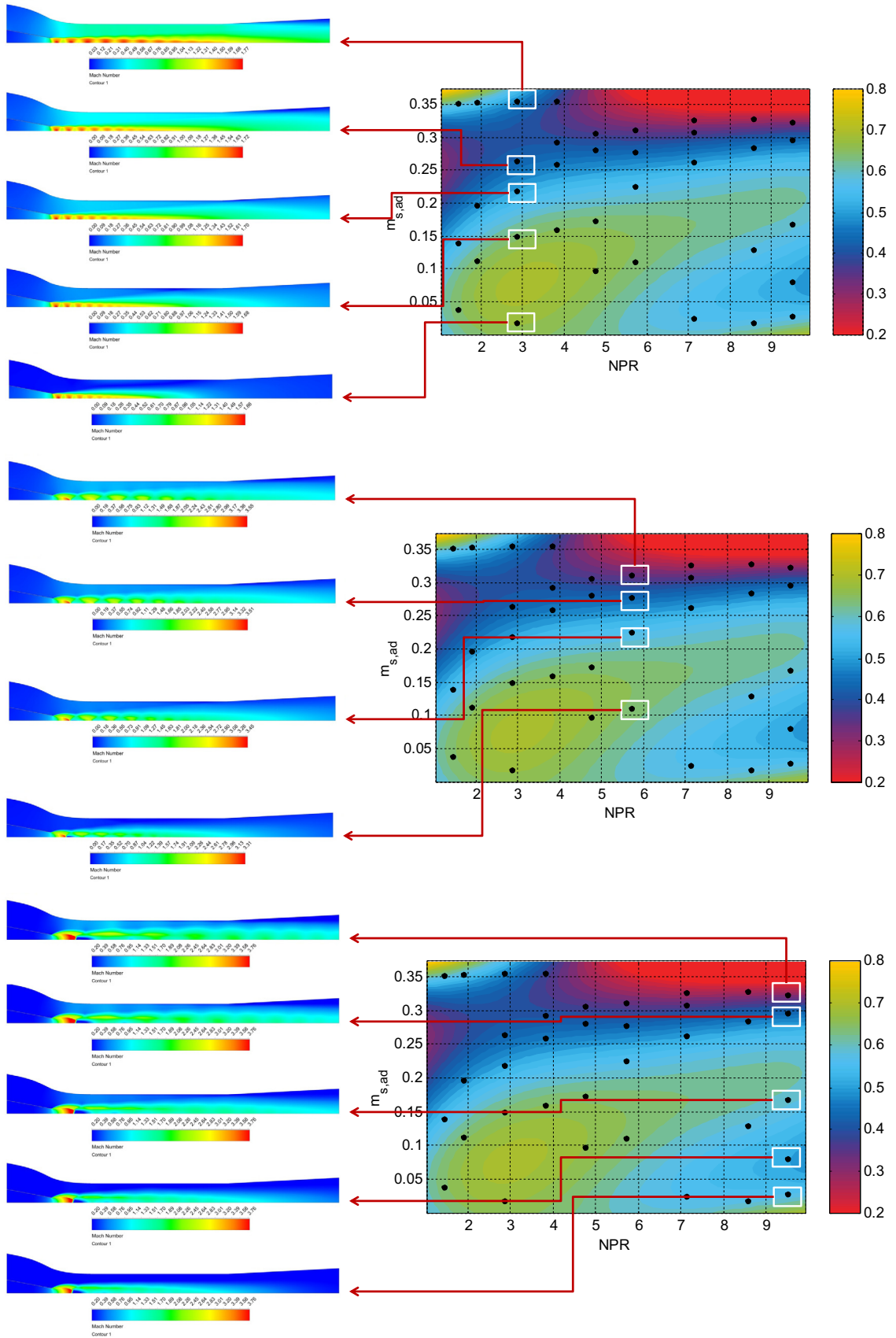**Fig. 7.** Mixing chamber: relations between efficiencies and flow phenomena.

Fig. 8. Diffuser: relations between efficiencies and flow phenomena.

Table 1
Ejector component efficiencies: regressing equations (air as working fluid).

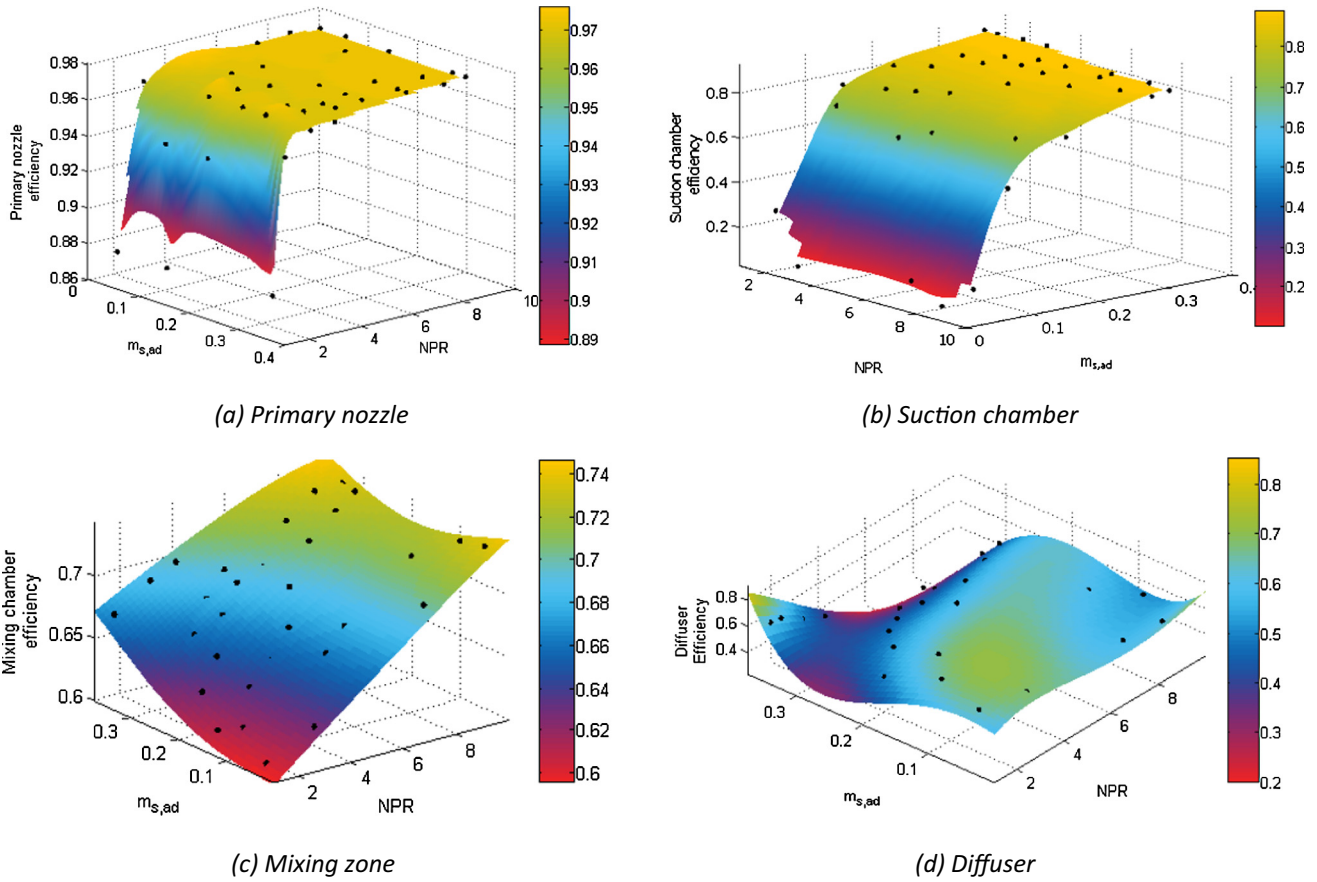| Zone	Correlations	RMSE
Primary nozzle	$\eta_p = 0.969e^{0.00043NPR} - 6.214e^{-2.93NPR}$	0.9925
Suction chamber	$\eta_s = 0.864e^{0.0832m_{s,ad}} - 1.083e^{-16.41m_{s,ad}}$	0.9981
Mixing chamber	$\eta_{mix} = 0.5761 + 0.01995NPR - 0.0275m_{s,ad} - 0.0008652NPR^2 + 0.02206NPR * m_{s,ad}$ $-0.08955m_{s,ad}^2 + 0.000142NPR^3 - 0.002835NPR^2m_{s,ad} + 0.1431NPRm_{s,ad}^2$ $-3.503m_{s,ad}^3 - 0.000005837NPR^4 - 0.00008721NPR^3m_{s,ad} + 0.009375NPR^2m_{s,ad}^2$ $+0.08513NPRm_{s,ad}^3 - 5.059m_{s,ad}^4$	0.9981
Diffuser	$\eta_{diff} = 0.9655 + 0.2338NPR - 11.17m_{s,ad} - 0.1215NPR^2 + 1.583NPR * m_{s,ad}$ $+67.38m_{s,ad}^2 + 0.01291NPR^3 - 0.02569NPR^2m_{s,ad} - 4.124NPRm_{s,ad}^2$ $-259.4m_{s,ad}^3 - 0.0003611NPR^4 - 0.0164NPR^3m_{s,ad} + 0.6397NPR^2m_{s,ad}^2$ $-8.234NPRm_{s,ad}^3 - 437.1m_{s,ad}^4$	0.9825

(a) Primary nozzle

(b) Suction chamber

(c) Mixing zone

(d) Diffuser

Fig. 9. Ejector component efficiency maps.

Table 2
Ejector component efficiencies: regressing equations (Hydrogen as working fluid).

Zone	Correlations	RMSE [-]
Primary nozzle	$\eta_p = 0.967e^{0.002068NPR} - 6.311e^{-3.005NPR}$	0.9957
Suction chamber	$\eta_s = 5.765e^{-3.263m_{s,ad}} - 5.78e^{-4.989m_{s,ad}}$	0.9885
Mixing chamber	$\eta_{mix} = 5.7565 + 0.01836NPR + 0.06731m_{s,ad} - 0.0015NPR^2$ $-0.01775NPR * m_{s,ad} + 0.381m_{s,ad}^2$	0.9936
Diffuser	$\eta_{diff} = 5.6531 - 7.721NPR - 24.47m_{s,ad} + 3.87NPR^2 + 9.972NPR * m_{s,ad}$ $+121.2m_{s,ad}^2 + -0.832NPR^3 - 1.834NPR^2m_{s,ad} - 22.86NPRm_{s,ad}^2$ $-308.7m_{s,ad}^3 + 0.064NPR^4 + 0.155NPR^3m_{s,ad} - 0.17NPR^2m_{s,ad}^2 + 60.05NPRm_{s,ad}^3$	0.9530

and LPM models consider fluids with the same thermodynamic properties. The efficiency maps obtained by using air as working fluid have been applied in the 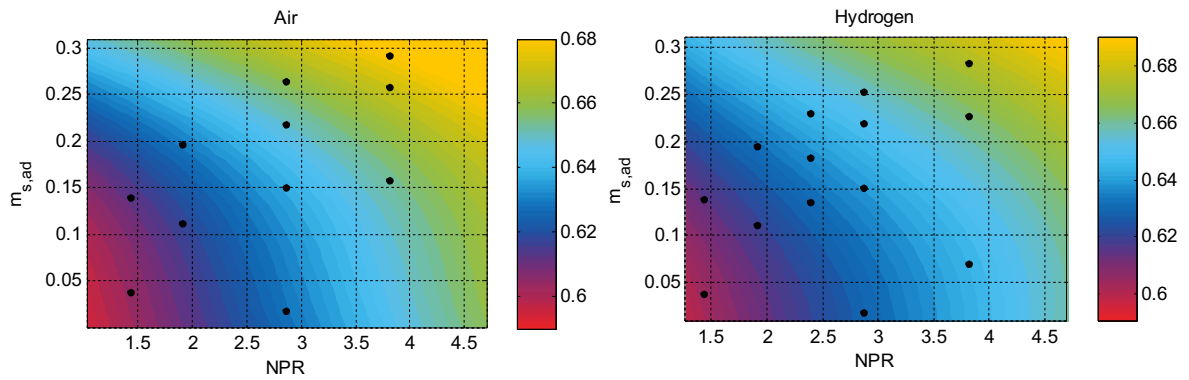following of the analysis. Indeed, we have verified (as detailed in Appendix B) that these maps have been representative also of the case of Hydrogen as working fluids (see also the discussion in Section 4.2.6).
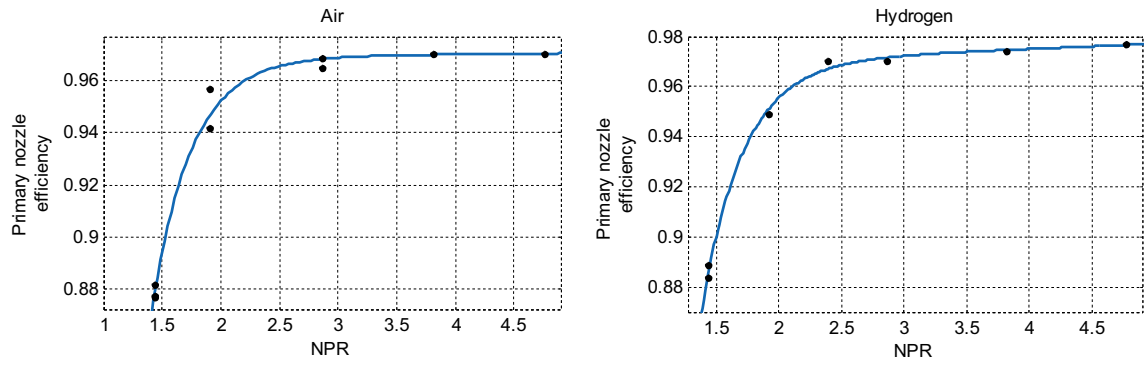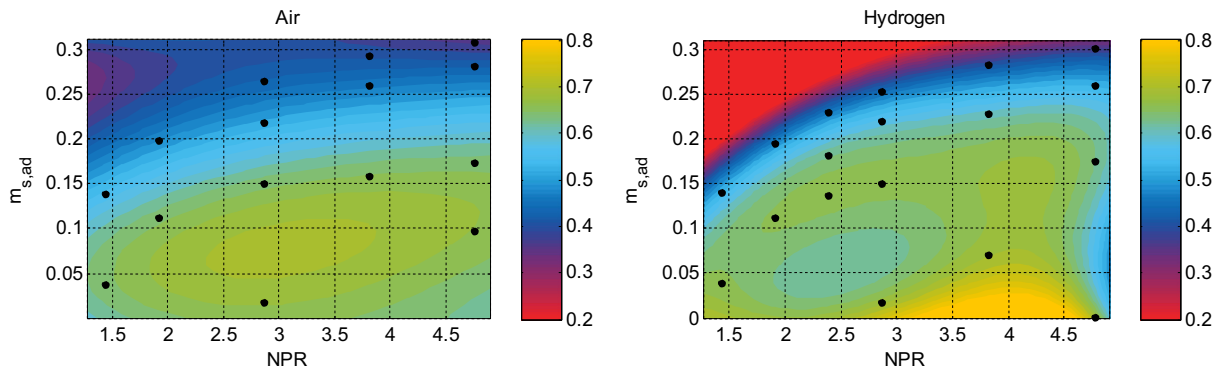
(a) Primary nozzle
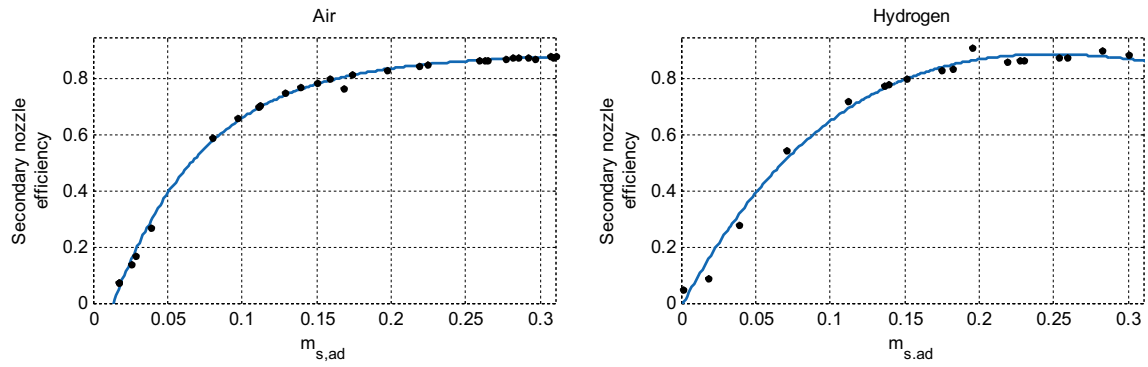
(b) Suction chamber

(c) Mixing zone

(d) Diffuser

Fig. 10. Influence of working fluid: comparison between air and Hydrogen.

5.2. ILPM-CFD model validation

The ILPM-CFD model has been validated by comparing its results to the ones obtained by the (validated) CFD approach. The results show that ILPM-CFD fits the CFD results data fairly well in the whole range of operating conditions (Fig. 11a–d). In particu-lar, Fig. 11a compared the ejector operating curves obtained by the CFD approach and the ILPM-CFD approach; conversely, Fig. 11b and c displays the parity plots for the primary and sec-ondary mass flow rate, respectively. In addition Fig. 11d display a parity plot for the onset of the back flow conditions, in terms of the back-pressure. The mean relative error in the primary mass-flow rate is below 1% (Fig. 11b), whereas, the relative error in the secondary mass-flow rate (Fig. 11c) is slightly higher (generally, below 5%) and is larger near to the back-flow condition. Moreover, the ILPM-CFD approach is able to detect the onset of the back-flow conditions for the different conditions tested, as displayed in Fig. 11d (the mean relative error is below 1%).

5.3. ILPM-CFD model evaluation

In this section, the role of variable ejector component efficien-cies in the correct evaluation of the ejector performance, when using LPM models, have been studied. In particular, the perfor-mance of the ILPM-CFD approach has been compared with the per-formance of (a) Constant Efficiencies Model (CEM) and (b) Constant-pressure CEM (CCEM), built as follows:

1. the constant efficiency model (CEM) has been build using the same structure of the ILPM-CFD, but without implementing a variable formulation for ejector component efficiencies. Hence, only LPM equations have been solved in a sequential way and constant ejector component efficiencies have been used. The efficiencies used in this case ($\eta_p = 0.97$, $\eta_s = 0.9$, $\eta_{mix} = 0.65$ and $\eta_d = 0.7$) are the average values of the variable efficiency maps. They are within the range of variability reported in the litera-ture [15–17,39] and consistent with the most common litera-ture ejector component efficiencies [40–45].

2. a Constant-pressure CEM (CCEM) has been developed to evalu-ate the whole operating range of a convergent-nozzle ejector. This model has been described in the Appendix C.

Fig. 12 and Fig. 13 display the results of this comparison; in par-ticular, in Fig. 12, lines are for the model and dots are CFD simula-tions. Conversely, Fig. 13 presents a parity plot, which compares the secondary mass flow rate obtained by the CFD approach and by the lumped parameter models (ILPM-CFD, CEM and CCEM mod-els). The CEM model has been not able to correctly describe the behavior of the ejector in the whole operating range (Fig. 12a and Fig. 13): (a) the CEM model has been able to predict the CFD data only for small- or average-under-expanded jet (where the constant ejector component efficiencies chosen are reliable); (b) conversely, the CEM model is unable to correctly predict the ejec-tor performance in the case of sub-sonic flow field or highly under-expanded jet (owing to the value chosen of the ejector component efficiencies). On the contrary, the CCEM model has been able to describe the ejector performance in limited range of operating con-ditions (Fig. 12b and Fig. 13). In particular, the CCEM model is able to describe the ejector behavior only for intermediate operating conditions. The errors become higher (i) near back flow, for (ii) highly under-expanded jet and for (iii) high primary flow pres-sure/low back-pressure:

1. **back flow conditions.** The use of constant efficiencies smooth sudden effects as the secondary mass-flow rate drop near the back-flow and secondary mass flow rate is over estimated.

Moreover, the back flow pressure is modeled using a separate procedure. These two reasons cause the sudden change in slope of the secondary mass flow;

2. **highly under-expanded jet.** The usage of constant efficiencies brings to an over-estimation of the secondary mass-flow rate;

3. **high primary flow pressure and low back-pressure.** The model under-predict the secondary mass-flow rate. This is because model predicts the secondary flow chocking, which does not occur.

We may conclude that a constant efficiency model is unable to reproduce the ejector performance in the whole operating range because ejector component efficiencies vary significantly in the range of analysis. Therefore, CEM models should be used carefully and they should be used only for the evaluation of ejectors in on-design operation mode or in a very narrow range of operating con-ditions. In the latter case, efficiencies should be carefully evaluated before using the model. Conversely, ILMP-CFD is able to calibrate the value of efficiency in each operating condition. In this frame-work, ejector component efficiencies are not only a way to intro-duce irreversibility in lumped parameter models, but also a way to taking into account local flow behavior in lumped parameter model. In Section 6, the influence of ejector models is evaluated in terms of the capability prediction of an ejector-based system.

## 6. PEMFC recirculation system modeling and analysis

The ILPM-CFD model has been applied to study an ejector-based anode recirculation in a proton exchange membrane fuel cell sys-tem. In this section, the implementation of the models involving both fluid dynamics and electro-chemical analysis has been described. First, the PEMFC system has been presented; second, the integration of the ejector model on the PEMFC model has been described; third, the electro-chemical fuel cell model has been dee-ply described. Finally, the simulation results have been presented and commented.

6.1. PEMFC recirculation system description

Fig. 1a displays the PEMFC system considered, along with the integration with the ejector component. This PEMFC system has been taken from the literature (see Refs. [10,11,46,47]). In particu-lar, for comparison purposes, the same PEMFC studied by Zhu et al. [47] has been used also in this study; in addition, data and infor-mation concerning the geometry of the channels have been taken from Refs. [48] and have been listed in Table 3. Taking into account the geometrical parameters of the fuel cell, the geometry of the ejector has been modified to fit fuel cell mass-flow rates; in this respect, the geometry of the ejector has been modified keeping geometrical and fluid dynamic similitude. The interested reader may refer to the other papers for a more detailed discussion con-cerning the influence of the fuel cell geometry and design on the system performance (for example, Refs. [3,49,50]).

6.2. ILPM-CFD ejector model within the PEMFC system: Integrated solving procedure

In order to simulate an ejector-based system (in this case, a PEMFC system with an ejector on the anodic recirculation line), the ejector model (and its solving procedure) must be coupled with the other components in the system. The coupling between the ejector model and the fuel cell model has been obtained by employing appropriate boundary conditions: in a PEMFC recircula-tion system, the ejector should raise the secondary flow pressure ($\Delta p_{ejector}$) to balance the pressure loss in the fuel cell (Δp_{loss}). Tak-
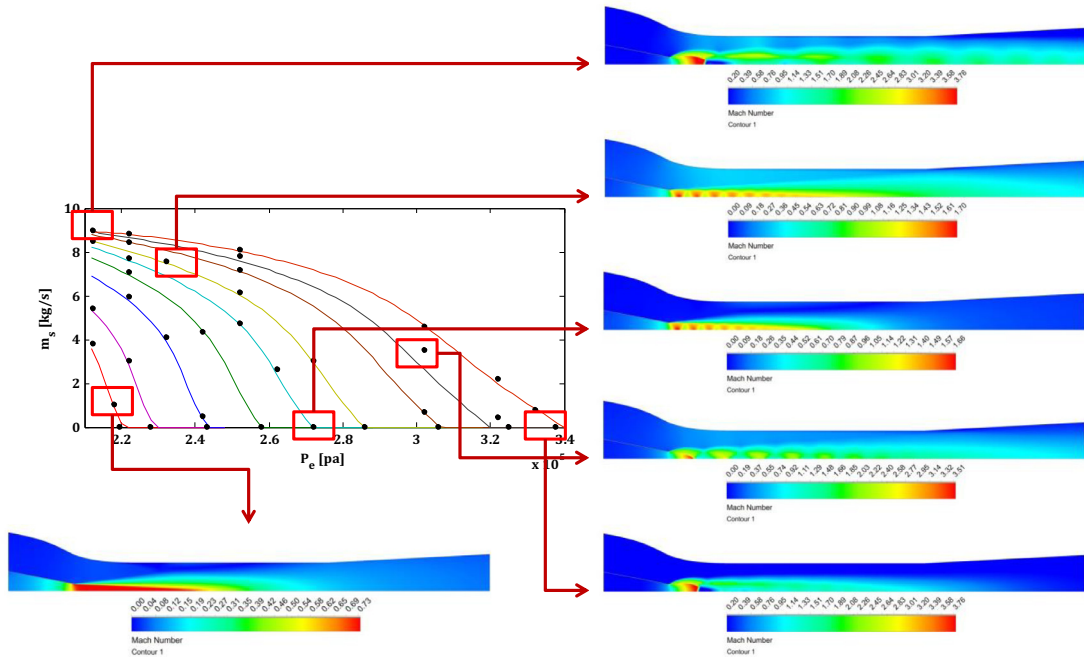
(a) Ejector operating curve prediction
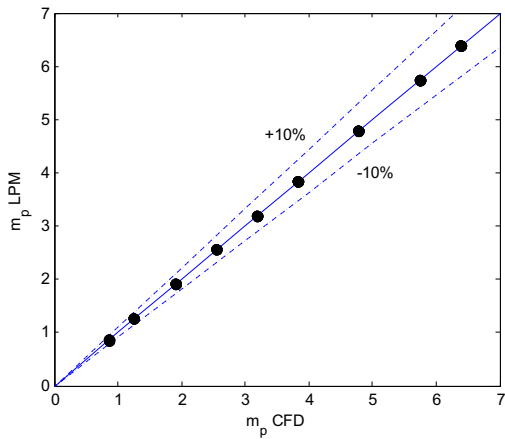
(b) Primary mass flow rate: parity plot
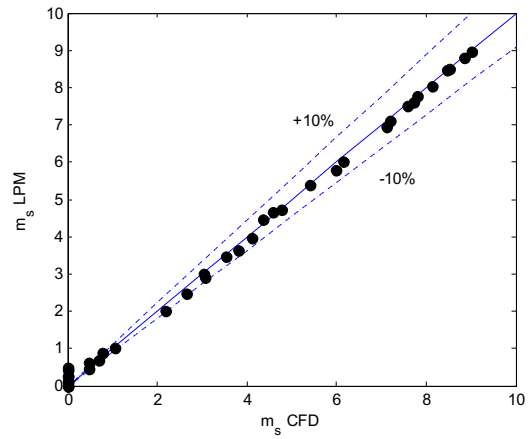
(c) Secondary mass flow rate: parity plot

(d) Back-pressure for the onset of the back flow: parity plot

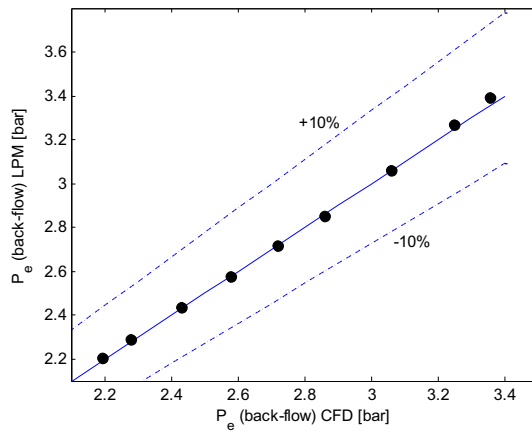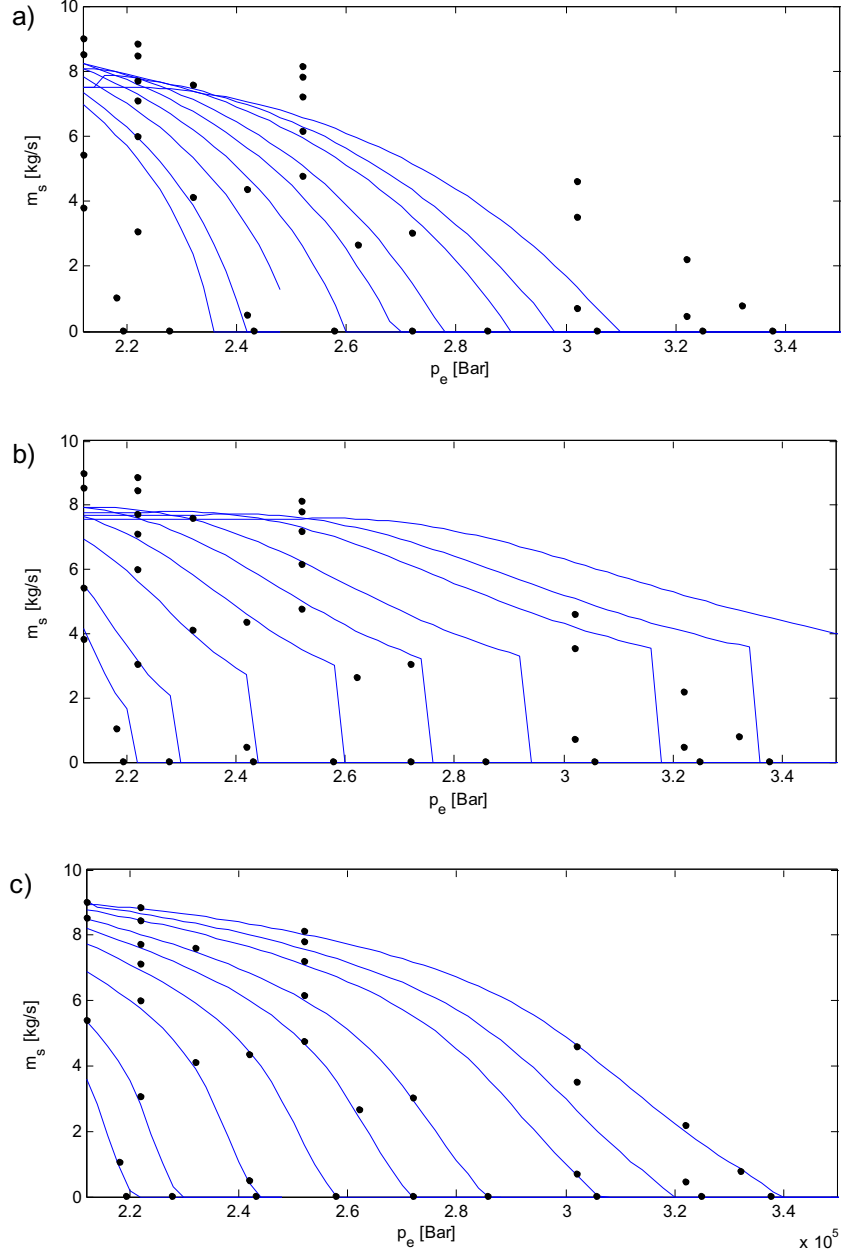**Fig. 11.** ILPM-CFD performance and comparison with CFD results.

Fig. 12. Comparison of ejector models: a) CEM, b) CCEM c) ILPM-CFD (lines are for the lumped parameter model and dots are CFD simulations).

ing into account this concept, the solving procedure of the ejector (when coupled with PEMFC system) is as follows:

1. the secondary mass-flow rate is initialized and the LPM is solved to obtain p_e and, thus, $\Delta p_{ejector} = p_e - p_{s,in}$;
2. the pressure drop Δp_{cell} across the fuel cell is computed (as described by the fuel cell model in Section 6.3.2);
3. the difference between the pressure raise inside the ejector ($\Delta p_{ejector}$) and the pressure loss in the fuel cell (Δp_{loss}) is computed: if $\Delta p_{ejector} < \Delta p_{cell}$, the ejector compresses the stream less than required and entrained mass-flow rate is reduced (or vice versa):

$$m_{s,i+1} = m_{s,i}\left[1 + k\left(\frac{\Delta p_{ejector}}{\Delta p_{cell}} - 1\right)\right] \qquad (24)$$

In Eq. (24) k is the relaxation factor that could be used to improve the convergence behavior of the model (in the present study,

$k = 0.9$). The above-mentioned procedure has been iterated until convergence, which is supposed to be reached when residuals are less than 10^{-6}. The ILPM-CFD model detects a back-flow condition when the ejector is not able to balance Δp_{cell}, thus resulting in negative secondary mass flow rate. The outputs of the above-mentioned solving procedure consist in (a) the primary mass flow rate ($\dot{m}_p$) and (b) the secondary mass flow rate ($\dot{m}_s$).

6.3. PEMFC model

In this section, the fuel cell model (which has been coupled with the ejector model) has been presented.

6.3.1. PEMFC Model: The assumptions

The aim of the proposed investigation is to study the performance of the fuel delivery and the anode recirculation lines; in this respect, only the performance of anode side has been considered and analyzed (see also Ref. [47]). It is worth noting that a compre-
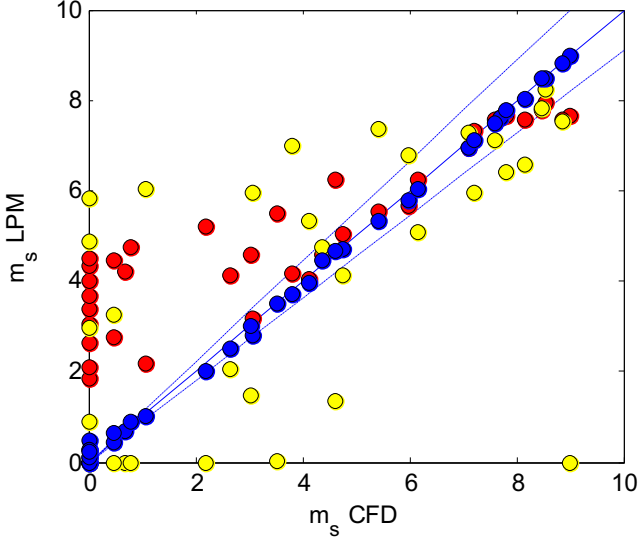
Fig. 13. Comparison of ejector models: secondary mass flow rate parity plot.

Table 3
Inputs of the fuel cell model.

	Parameter	Value
A_{cell}	Cell active area	0.1 [m²]
N_{cell}	Cell number	381 [–]
L	Membrane thickness	127 [μm]
$T_p = T_{H2}$	Hydrogen inlet temperature	298 [K]
T_s	Secondary flow temperature	353 [K]
T_{cell}	Stack operating temperature	353 [K]
P_{cell}	Fuel cell pressure	3 [bar]
$A_{t,p}$	Primary nozzle	0.12 [cm²]
$A_{s,p}$	Secondary nozzle	2.94 [cm²]
A_{mix}	Constant area section	1.81 [cm²]
$N_{channel}$	Number of channels	50 [–]
b	Channel width	1 [mm]
i	Channle height	1 [mm]
d	Channel distance	1 [mm]

hensive evaluation of PEMFC system performance is far beyond the scope of this paper, which aim to describe the implementation of ejector models in PEMFC systems. The main assumptions employed in this study (in agreement with the literature, see Ref. [47]) are as follows:

1. the humidity of the fuel cell has been controlled by the cathodic mass-flow rate, therefore, we have considered the anodic side fed only by hydrogen;
2. the cathode side of the fuel cell has been not taken into account;
3. the properties of the fluids have been taken as constant;
4. the cell has been considered working at a uniform and constant temperature;
5. the secondary effects have been neglected (i.e. water transport from the cathode to the anode).

6.3.2. Fuel cell pressure drop model
The total pressure drop in fuel cell has been computed as follows [51]:

$$\Delta p_{cell} = f \frac{L}{D_h} \rho \frac{v^2}{2} + \sum k_l \rho \frac{v^2}{2} \tag{25}$$

The first term, on the right side of Eq. (25), represents the pressure loss due to the wall friction, whereas the second term, on the right side of Eq. (25), represents the pressure loss due to the local effects.

In this paper, the second term has been neglected, being the detailed study of the fuel cell system far beyond the purpose of this paper. Future researchers may easily extend the proposed model to complex fuel system design, by taking into account this term (once the complete design of the fuel cell is known).

In Eq. (25), D_h is the hydraulic diameter of the channels and, considering rectangular section channels, it reads as follows:

$$D_h = \frac{2(b+i)^2}{b+i} \tag{26}$$

where b and i represent the fuel cell channel height and width. The velocity inside every channel, v, has been computed as follows:

$$v = \frac{\dot{m}_{cell}}{\rho N_{cell} N_{channel} A_{channel}} \tag{27}$$

In the channels of a PEMFC, the flow is—generally—laminar ($Re <$ 2300, where Re is the Reynolds number); therefore the friction coefficient, f, has been given by [48]:

$$f = \frac{55 + 41.5 e^{(-3.4b/i)}}{Re} \tag{28}$$

In the present case, $f = 56.38/Re$.
Therefore, from Eq. (25) follows Eq. (29):

$$\Delta p_{cell} = \frac{28.19}{Re\rho} \frac{L}{D_h} \left(\frac{\dot{m}_{cell}}{N_{cell} N_{channel} A_{cell}} \right)^2 \tag{29}$$

Eq. (29), to compute the pressure losses in the fuel cell has been provided as boundary condition in the ejector-based system solving procedure (please refer to Section 6.2).

6.3.3. Fuel cell electro-chemical model
The voltage, V_{cell}, of a generic fuel cell has been given by [52]:

$$V_{cell} = E + \eta_{act,c} + \eta_{act,a} + \eta_{ohmic} + \eta_{conc} \Rightarrow^{Hypotesis2} E + \eta_{act,a}$$
$$+ \eta_{ohmic} + \eta_{conc} \tag{30}$$

Where E is the thermodynamic potential, $\eta_{act,a}$ is the anode activation overvoltage, $\eta_{act,c}$ is the cathode activation overvoltage (this contribution has been neglected owing to hypothesis #2), η_{ohmic} is the ohmic overvoltage and η_{conc} is the concentration overvoltage.

Once V_{cell} is known (see the next sections), the fuel cell performances can be computed as follows [53]:

$$P_{cell} = V_{cell} I_{cell} \tag{31}$$

$$\eta_{cell} = \frac{2 N_{cell} V_{cell} I_{cell}}{\dot{m}_{H_2,reacted} LHV_{H_2}} \tag{32}$$

where $m_{H2,reacted}$ is the mass-flow rate of hydrogen consumed in the anode-side of the fuel cell:

$$\dot{m}_{H_2,reacted} = \frac{N_{cell} I_{cell} MM_{H_2}}{2F} \tag{33}$$

In Eq. (33) F is the Faraday constant (96,487 C/mol).
In the following sub-sections, the mathematical formulation of the different terms appearing in the right side of Eq. (30) has been provided, discussed and referenced.

6.3.3.1. Thermodynamic potential.
The thermodynamic potential of the hydrogen oxidation reaction has been computed by using the well-known Nerst law, which reads as follows:

$$E = 1,229 - 0,85 \times 10^{-3}(T_{cell} - 298,15) + 4,3085$$
$$\times 10^{-5} T_{cell} \log[p_{H_2}^* p_{O_2}^{*0.5}] \tag{34}$$

where p_{H2}^* and p_{O2}^* are the partial pressures of hydrogen at the anode/catalyst interface and oxygen at the cathode/catalyst inter-

face, respectively. Generally, the evaluation of p_{H2}^* and p_{O2}^* partial pressures involves mass transfer calculations and normally requires averaging over a cell surface or along the direction of gas flow, to account for significant changes in the bulk phase partial pressures of the gaseous reactants due to reaction in the cell [54]. In the present case they have been computed by using the following equations (see Ref. [54]):

$$p_{O_2}^* = p \left[1 - x_{H_2O}^{sat} - x_{othergasses}^{channel} \exp \left(\frac{0.291 I_{cell}/A_{cell}}{T_{cell}^{0.832}} \right) \right] \tag{35}$$

$$p_{H_2}^* = 0.5 p_{H_2O}^{sat} \left\{ 1 \left/ \left[\exp \frac{1.653 I_{cell}/A_{cell}}{T_{cell}^{1.334}} \right) x_{H_2O}^{sat} \right] - 1 \right\} \tag{36}$$

where $x_{othergasses}^{channel}$ is the molar fraction of the other gases (apart from oxygen) in the air steam, and $x_{H_2O}^{sat}$ is the molar fraction of the water in a gas stream at saturation for a given temperature:

$$x_{H_2O}^{sat} = p_{H_2O}^{sat}/p \tag{37}$$

where the saturation pressure of water vapor, $p_{H_2O}^{sat}$, has been computed as follows:

$$\ln(p_{H_2O}^{sat}) = 70.4346 - 7362.6981/T_{cell} + 66.9521 \cdot 10^{-3} T_{cell} \\ - 9.0 \ln(T_{cell}) \tag{38}$$

Finally, $x_{othergasses}^{channel}$ is given by a logarithmic mean average between the molar fraction of other gases apart from oxygen in a humidified stream of air at the inlet, $x_{othergasses}^{in,hum}$, and outlet, $x_{othergasses}^{out,hum}$, of cathode side [46]:

$$x_{othergasses}^{channel} = \frac{x_{othergasses}^{in,hum} - x_{othergasses}^{out,hum}}{\ln(x_{othergasses}^{in,hum}/x_{othergasses}^{out,hum})} \tag{39}$$

where $x_{othergasses}^{in,hum}$ and $x_{othergasses}^{out,hum}$ reads as follows:

$$x_{othergasses}^{in,hum} = 0.79(1 - x_{H_2O}^{sat}) \tag{40}$$

$$x_{othergasses}^{out,hum} = \frac{1 - x_{H_2O}^{sat}}{1 + [1 - (1/x_{air})](0.21/0.79)} \tag{41}$$

6.3.3.2. Anode overvoltage. The expression of the anode overvoltage, $\eta_{act,a}$, has been provided by a (semi-empirical) expression [52]:

$$\eta_{act,a} = \xi_1 + \xi_2 T_{cell} + \xi_3 T_{cell} \log(C_{O_2}^*) + \xi_4 T_{cell} \log(I_{cell}) \tag{42}$$

where C_{O2}^* is the oxygen concentration at the membrane/gas interface:

$$C_{O_2}^* = 1.97 \cdot 10^{-7} \exp(498/T_{cell}) p_{O_2}^* \tag{43}$$

The values of the above coefficient have been taken from literature and they read as follows [52]: (a) $\xi_1 = -0.9154$, (b) $\xi_2 = 0.00312$, (c) $\xi_3 = 0.000074$ and (d) $\xi_4 = -0.0003187$.

6.3.3.3. Ohmic resistance. The ohmic resistance, η_{ohmic}, can be written through the Ohm's Law equations as:

$$\eta_{ohmic} = -I_{cell} R_{proton} \tag{44}$$

An expression for the internal resistance was proposed by Mann [52] to include all the important membrane parameters and has been applied in this paper:

$$R_{proton} = \frac{r_M l_{membrane}}{A_{cell}} \tag{45}$$

where r_M is the membrane specific resistivity for the flow of hydrated protons, l is the thickness of the polymer membrane

(127 μm in our case NAFION 117). The expression to compute r_M is as follows (see Ref. [52]):

$$r_M = \frac{181,6 \left[1 + 0.03 \left(\frac{I_{cell}}{A_{cell}} \right) + 0,062 \left(\frac{T_{cell}}{303} \right)^2 \left(\frac{I_{cell}}{A_{cell}} \right)^{2,5} \right]}{\left[\lambda - 0.634 - 3 \left(\frac{I_{cell}}{A_{cell}} \right) \right] \exp \left(4.18 \left[\frac{T_{cell}-303}{T_{cell}} \right] \right)} \tag{46}$$

where λ is an empirical parameter and a constant value ($\lambda = 23$ [52]) has been used.

6.3.3.4. Concentration overvoltage. The concentration overvoltage, η_{conc}, has been modeled by using the following equation, Eq. (47):

$$\eta_{conc} = g_1 \exp(g_2 \cdot I_{cell}) \tag{47}$$

where g_1 and g_2 are the mass transfer coefficient the growth rate of byproducts of the electrochemical reaction in the catalyst layers, flow fields, and across the electrode. Laurencelle et al. [55] have proposed g_2 between 0.007 and 0.009. A partially dehydrated electrolyte membrane leads to a decrease in conductivity, which can be represented by mass transfer coefficient, g_1, which depends on the fuell cell temperature as follows:

$$g_1 = \begin{cases} 3.3 \cdot 10^{-3} - 8.2 \cdot 10^{-5}(T_{cell} - 273.15) & T_{cell} \leqslant 312.15 \text{ K} \\ 1.1 \cdot 10^{-4} - 1.2 \cdot 10^{-6}(T_{cell} - 273.15) & T_{cell} \geqslant 312.15 \text{ K} \end{cases}$$

$$\tag{48}$$

6.4. PEMFC simulation results

The performances of the whole PEMFC system (considering both the full cell stack and the ejector recirculation) have been ana-lyzed by varying the stack current, I_{cell}. Indeed, the stack current is a fuel cell parameter, which represents the load of the full cell (as clearly observed in the above-mentioned equations). It is worth noting that a comprehensive evaluation of PEMFC system perfor-mance is far beyond the scope of this paper, which aims (a) to describe the implementation of ejector models in PEMFC systems and (b) to discuss the influence of ejector modeling (i.e., constant and variable ejector component efficiency models) to predict the performance of the whole systems. Fig. 14 displays the results of the proposed analysis, which have been discussed in the following. Fig. 14a presents the fuel cell parameters and, in particular, it displays the relationship between the stack current and (a) the pri-mary flow pressure and (b) the pressure drop across the fuel cell. The primary flow pressure increases while increasing I_{cell}; conse-quently, the mass-flow rate of the hydrogen increases while increasing the primary flow pressure (which is the motive pres-sure) (Fig. 14a). This result is related to the physical interpretation of the ejector operating curves discussed in the previous sections. In addition, the pressure lift provided by the ejector increases while increasing I_{cell}, (Fig. 14a): this result is somehow expected because the pressure drop in the fuel cell is related with the mass flow rate (please refer to Eq. (29)). The fuel cell parameters (pre-sented in Fig. 14a) can be related to the ejector performances by considering the results in Fig. 14b and in Fig. 14c. In particular, Fig. 14b displays the relationship between the primary flow pres-sure and (a) the entrainment ratio and (b) the outlet/discharged temperature. In particular, the entrainment ratio decreases while increasing the primary flow pressure, because the primary mass flow rate increase; the outlet temperature has a trend similar to the one of the entrainment ratio, (Fig. 14b). Conversely, Fig. 14c displays the relationship between the primary flow pressure and (a) the primary mass flow rate (m_p) and (b) the secondary mass flow rate (m_s). The curve of the primary mass flow rate has differ-ent shapes (Fig. 14c) according to the motive nozzle fluid dynamic
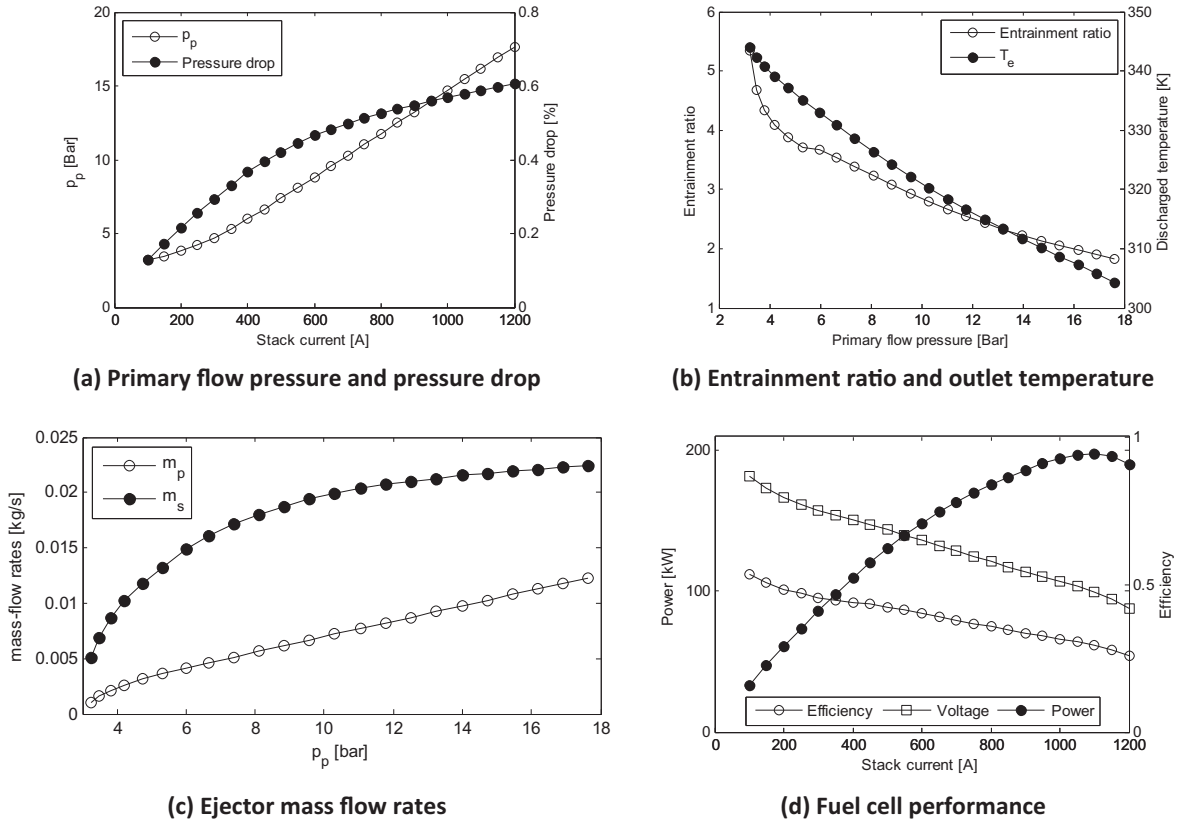
(a) Primary flow pressure and pressure drop

(b) Entrainment ratio and outlet temperature

(c) Ejector mass flow rates

(d) Fuel cell performance

Fig. 14. PEMFC system: simulation results.

operation (i.e., chocked flow or not-chocked flow). This behavior and the trends of m_p and m_s are very similar to previous experimental and numerical results (see, for example, the results presented in Refs. [47,56,57]) and similar comments also apply in the present case. Finally, Fig. 14d displays the relationship between the stack current (I_{cell}) and the fuel cell performance parameters:(a) the fuel cell power (as defined in Eq. (31)) and (b) the fuel cell efficiency (as defined in Eq. (32))). The fuel cell efficiency decreases while increasing the stack current; conversely, the fuel cell power increases till a maximum value has been reached (Fig. 14d). The maximum value of the fuel cell power is caused by the trade-off between the stack current and voltage. This behavior agrees with the well-known performance characteristics of a typical PEM fuel cell stacks.

It is worth noting that the present ejector is not always able to guarantee the optimal entrainment ratio for the fuel cell. Indeed, the entrainment ratios of the proposed ejector are quite high if compared to typical PEM operations. This is because the hydrogen stoichiometric ratio changes with a trend similar to the ejector entrainment ratio (this issue has been discussed in Ref. [47]). A larger entrainment ratio (which results in more unconsumed hydrogen recycled) leads to larger hydrogen stoichiometric ratio. In order to adjust the hydrogen stoichiometric ratio, a regulation device can be used. For example, a throttle valve in the anodic recirculation line can be used to regulate the secondary flow pres-sure in order to meet the required entrainment ratio. In this case the ejector behavior would be guaranteed by the fixed pressure drop in the anodic recirculation line and, as a results, the secondary flow pressure reduces according to the requested entrainment ratio (Fig. 15). Generally, these results confirm that ejector is a crit-ical component in the design of energy systems: a small deviation from the optimum operating conditions of the ejector might dras-tically lower the performances of the whole system.

6.5. Comparison with constant efficiency models

In the previous Section 6.4, the PEMFC system has been simulated and the ILPM-CFD approach has been applied to model the ejector behavior in this system. In this section, the role of the ejector model and, in particular, the role of the ejector component efficiency values has been investigated. In particular, the models presented in Section 5.2 have been compared to the ILPM-CFD model, when coupled with the aforementioned fuel cell system. As a result, Fig. 16 displays the outcomes of this analysis; in particular, Fig. 16 relates the stack current (I_{cell}) to the fuel cell power (Eq. (31)). The ILMP-CFD model and the CCEM model describe the same ejector behavior in a broad range of fuel cell operating conditions; however, the ILMP-CFD model and the CCEM model
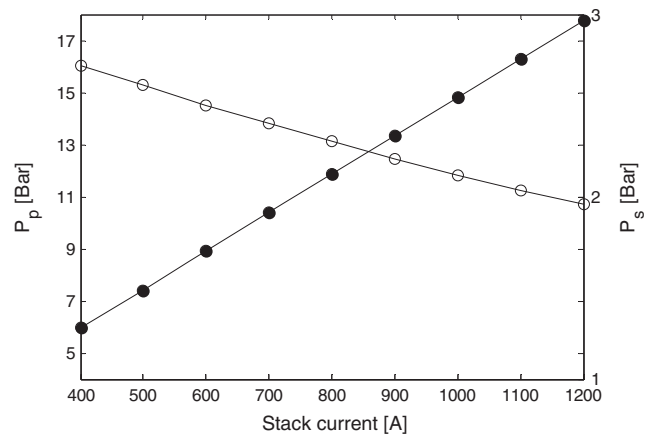

Fig. 15. Primary and secondary flow pressures – fixed fuel utilization ratio.
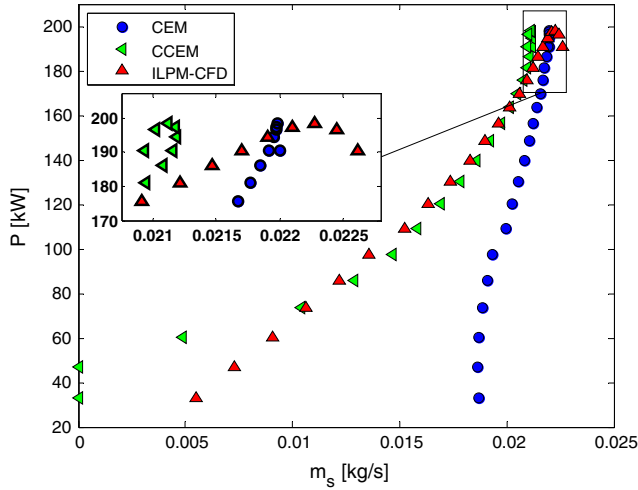
Fig. 16. PEMFC performances prediction using different ejector models.
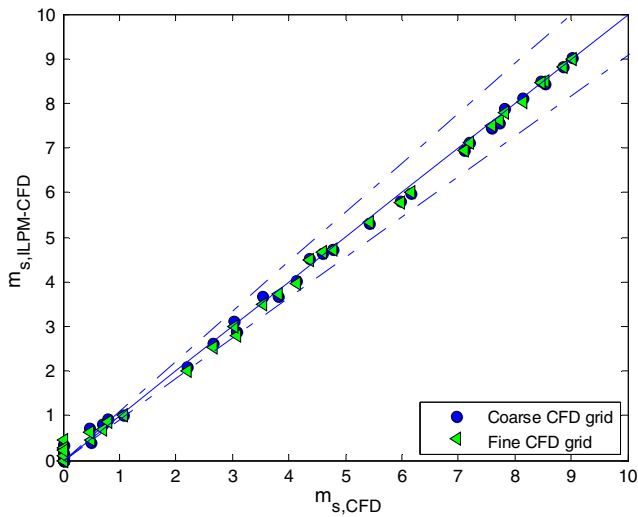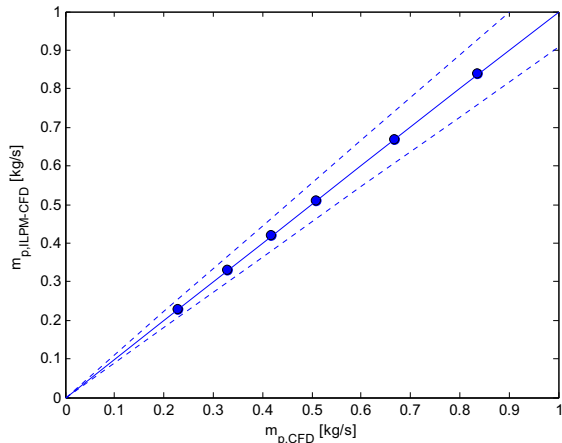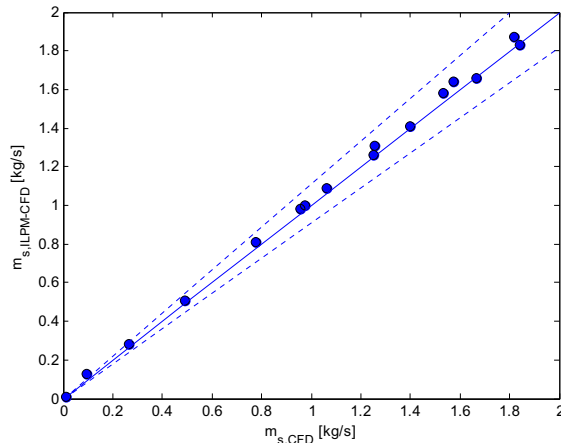

Fig. 17. CFD grid influence over ILPM-CFD results.

predict different behaviors at low stack current conditions and at high power conditions. Conversely, the CEM model predicts a completely different behavior and it over-estimates the entrained

mass-flow rate in the whole operating range. Indeed, CEM model, having constant ejector component efficiencies, has been not able to predict the off-design operation of the ejector. Therefore, it has been concluded that the correct modeling of the PEMFC system (in both on-design and off-design conditions) rely on multi-scale ejector modeling approaches.

7. Conclusions

We have applied an integrated lumped parameter- Computational Fluid Dynamics approach to investigate the performance of ejector for the anode recirculation in a proton exchange membrane fuel cell system.

The main outcomes of this study are as follows:

- the integrated lumped parameter-Computational Fluid Dynamics approach has shown better performance and a wider range of applicability compared with constant efficiency models, owing to its multi-scale approach.
- the integrated lumped parameter model- Computational Fluid Dynamics approach, due to the variable efficiency formulations, has been able to correctly consider the off-design performance of ejectors and ejector-based systems. Conversely, constant efficiency models have been unable to correctly predict the off-design performance of the fuel cell system.
- the results confirm that ejector is a critical component in the design of energy systems: a small deviation from the optimum operating conditions of the ejector might drastically lower the performances of the whole system.
- the correct modeling of ejector-based systems in both on-design and off-design conditions rely on multi-scale ejector modeling approaches.

Appendix A. Sensitivity analysis of the CFD grid for ejector component efficiencies

It is worth analyzing the influence of the number of points to build the maps of the ejector component efficiencies (the "*CFD grid for ejector component efficiencies*"). In the validation section (Section 5.2) we have used a fine "*CFD grid for ejector component efficiencies*" (45 simulation points), now LPM and CFD results have been compared using a coarse "*CFD grid for ejector component efficiencies*" (23 additional simulation points). The CFD simulation to build the coarse grid points have been chosen focusing on the

(a) Primary mass flow rate

(b) Secondary mass flow rate

Fig. 18. Comparison between CFD and model results using Hydrogen and air efficiency maps.
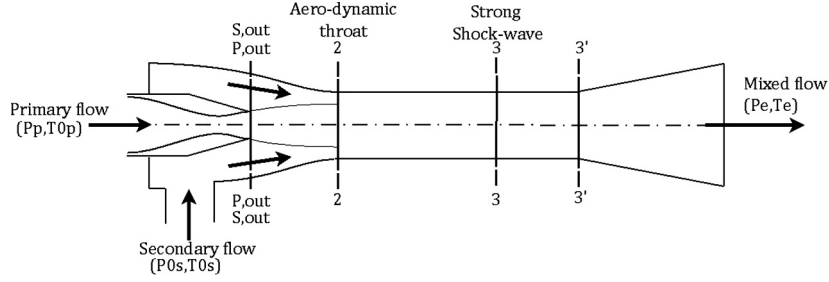
Fig. 19. CCEM Ejector layout.

points where little variation of operating conditions may led to a large variation of the performance (i.e. near the back-flow condition). The average error between CFD results and the ILPM-CFD model is 5.53% for the coarse CFD grid and 3.95% for the CFD fine grid. Therefore, we may conclude that the ILPM-CFD "converges" toward the correct solution (Fig. 17).

Appendix B. Hydrogen as working fluids

The capability of efficiency maps, obtained using air as the working fluid, to represent the behavior of the ejector with hydrogen have already been pointed out Section 4.2.6. However, in order to better justify this statement a validation by comparing CFD results using hydrogen as the working fluid and ILPM-CFD results using hydrogen as the working fluid but with efficiency maps calculated using air has been proposed. The results have been presented in Fig. 18 for the primary and the secondary flow. The mean error for the primary flow has been 0.56% and 3.51% for the secondary flow. These results further confirm the previous statement.

Appendix C. CCEM ejector model

Herein the CCEM model structure and its solving procedure have been presented. The reference ejector layout is presented in Fig. 19.

C.1. Model hypothesis

The model hypotheses are the same of the ILPM-CFD model:

1. ejector walls have been considered as adiabatic (isentropic relations can be used);
2. primary and the secondary fluids have been treated as ideal gases;
3. uniform velocity and thermodynamic conditions;
4. total conditions have been assigned at primary and secondary flow inlets.

C.2. Model structure

For a given inlet total pressure and temperature, the mass flow rate of the primary flow through the nozzle, has been obtained by using:

$$m_p = \frac{p_p A_t}{\sqrt{T_p}} \sqrt{\frac{\gamma}{R^*} \left(\frac{2}{\gamma+1}\right)^{\frac{(\gamma+1)}{(\gamma-1)}}} \sqrt{\eta_p} \tag{49}$$

The primary stream flows from the motive nozzle without mixing with the entrained flow; therefore, the primary flow between section out and 2 has been approximated with isentropic relations,

and the Mach number of the primary flow at Section 2 has been obtained:

$$\frac{p_{p,2}}{p_{p,out}} = \frac{\left[1 + \frac{\gamma-1}{2}M_{p,out}^2\right]^{\gamma/(\gamma-1)}}{\left[1 + \frac{\gamma-1}{2}M_{p,2}^2\right]^{\gamma/(\gamma-1)}} \tag{50}$$

The area of the primary flow at Section 2 can be calculated:

$$\frac{A_{p,2}}{A_{p,out}} = \frac{\frac{\phi_p}{M_{p,2}}\left[\frac{2}{\gamma+1}\left(1 + \frac{\gamma-1}{2}M_{p,out}^2\right)\right]^{(\gamma+1)/(2(\gamma-1))}}{\frac{1}{M_{p,out}}\left[\frac{2}{\gamma+1}\left(1 + \frac{\gamma-1}{2}M_{p,2}^2\right)\right]^{(\gamma+1)/(2(\gamma-1))}} \tag{51}$$

Primary flow temperature in the aero-dynamic throat has been obtained with:

$$\frac{T_p}{T_{p,2}} = 1 + \frac{\gamma-1}{2}M_{p,2}^2 \tag{52}$$

The solving procedure is different according to the operating condition (ejector working in critical or subcritical mode).

If secondary flow chokes at Section 2, following equations are valid:

$$M_{s,2} = 1 \tag{53}$$

$$p_{s,2}^* = p_{p,2} = p_s \left(\frac{2}{\gamma+1}\right)^{\gamma/(\gamma-1)} \tag{54}$$

$$m_s = \frac{p_s A_{s,2}}{\sqrt{T_s}} \sqrt{\frac{\gamma}{R^*} \left(\frac{2}{\gamma+1}\right)^{\frac{(\gamma+1)}{(\gamma-1)}}} \sqrt{\eta_s} \tag{55}$$

In this case flow velocity in the aero-dynamic throat is lower than the speed of sound. Using conservation of mass and energy, as well as isentropic relations, the following equations have been obtained:

$$p_{s,2} > p_{s,2}^* \tag{56}$$

The cross-section area of the secondary flow has been obtained with:

$$A_{p,2} + A_{s,2} = A_3 \tag{57}$$

Mixing process has been considered to take place at a constant pressure (CPM ejector), therefore, momentum balance in the mixing chamber can be written as follows:

$$\eta_{mix}(m_p v_{p,2} + m_s v_{s,2}) = (m_p + m_s)v_3 \tag{58}$$

$$m_p\left(c_{p,p}T_{p,2} + \frac{v_{p,2}^2}{2}\right) + m_s\left(c_{p,s}T_{s,2} + \frac{v_{s,2}^2}{2}\right)$$
$$= (m_s + m_p)\left(c_{p,3}T_3 + \frac{v_3^2}{2}\right) \tag{59}$$

Energy and mass balance have been then solved to find temperature and Mach number at the end of the mixing process.

In critical condition a normal shock has been supposed to occur, therefore pressure and Mach number at the end of the mixing chamber have been calculated as follows:

$$\frac{p_{3'}}{p_3} = 1 + \frac{2\gamma}{\gamma + 1}(M_3^2 - 1) \tag{60}$$

$$M_{3'}^2 = \frac{1 + \frac{\gamma - 1}{2}M_3^2}{\gamma M_3^2 - \frac{\gamma - 1}{2}} \tag{61}$$

Finally pressure recovery inside the diffuser has been calculated:

$$\frac{p_{3'}}{p_4} = \left(\eta_d \frac{\gamma - 1}{2}M_3^2 + 1\right)^{\frac{\gamma}{\gamma - 1}} \tag{62}$$

In case of back-flow condition, no secondary flow has been entrained inside the mixing chamber, therefore, the static pressure of the secondary flow inside the aero-dynamic throat can be considered equal to the secondary flow total pressure.

$$p_{p,2} = p_{s,2} = p_s \tag{63}$$

Hence, velocity and Mach number of the primary flow inside the aero-dynamic throat have been calculated using the same equations presented in Section 3. In back-flow condition, the velocity in the diffuser entrance cross-section is very low, therefore it can be considered equal to zero. In this case momentum and energy balance reduce to these two simple equations:

$$T_3 = T_{mix} = \frac{m_p \left(c_p T_{p,2} + \frac{u_{p,2}^2}{2}\right)}{c_p} \tag{64}$$

$$p_3 = \frac{(p_{p,2}A_{p,2} + m_p u_{p,2} + p_{s,2}A_{s,2})}{A_3} \tag{65}$$

References

[1] A.Z. Weber, R.L. Borup, R.M. Darling, P.K. Das, T.J. Dursch, W. Gu, D. Harvey, A. Kusoglu, S. Litster, M.M. Mench, R. Mukundan, J.P. Owejan, J.G. Pharoah, M. Secanell, I.V. Zenyuk, A critical review of modeling transport phenomena in polymer-electrolyte fuel cells, J. Electrochem. Soc. 161 (2014) F1254–F1299.

[2] M. Andersson, S.B. Beale, M. Espinoza, Z. Wu, W. Lehnert, A review of cell-scale multiphase flow modeling, including water management, in polymer electrolyte fuel cells, Appl. Energy 180 (2016) 757–778.

[3] H.-W. Wu, A review of recent development: transport and performance modeling of PEM fuel cells, Appl. Energy 165 (2016) 81–106.

[4] M. Carmo, D.L. Fritz, J. Mergel, D. Stolten, A comprehensive review on PEM water electrolysis, Int. J. Hydrogen Energy 38 (2013) 4901–4934.

[5] G. Besagni, R. Mereu, F. Inzoli, Ejector refrigeration: a comprehensive review, Renew. Sustain. Energy Rev. 53 (2016) 373–407.

[6] G. Angelino, C. Invernizzi, Ejector-assisted liquid metal topping cycles, Proc. Inst. Mech. Eng., Part A: J. Power Energy 218 (2004) 111–121.

[7] Y. Liao, D. Lucas, Computational modelling of flash boiling flows: a literature survey, Int. J. Heat Mass Transf. 111 (2017) 246–265.

[8] M. Kim, Y.-J. Sohn, C.-W. Cho, W.-Y. Lee, C.-S. Kim, Customized design for the ejector to recirculate a humidified hydrogen fuel in a submarine PEMFC, J. Power Sources 176 (2008) 529–533.

[9] J. He, S.-Y. Choe, C.-O. Hong, Analysis and control of a hybrid fuel delivery system for a polymer electrolyte membrane fuel cell, J. Power Sources 185 (2008) 973–984.

[10] C. Bao, M. Ouyang, B. Yi, Modeling and control of air stream and hydrogen flow with recirculation in a PEM fuel cell system—I. Control-oriented modeling, Int. J. Hydrogen Energy 31 (2006) 1879–1896.

[11] Y. Zhu, Y. Li, New theoretical model for convergent nozzle ejector in the proton exchange membrane fuel cell system, J. Power Sources 191 (2009) 510–519.

[12] D.A. Brunner, S. Marcks, M. Bajpai, A.K. Prasad, S.G. Advani, Design and characterization of an electronically controlled variable flow rate ejector for fuel cell applications, Int. J. Hydrogen Energy 37 (2012) 4457–4466.

[13] A. Maghsoodi, E. Afshari, H. Ahmadikia, Optimization of geometric parameters for design a high-performance ejector in the proton exchange membrane fuel cell system using artificial neural network and genetic algorithm, Appl. Therm. Eng. 71 (2014) 410–418.

[14] G. Besagni, R. Mereu, P. Chiesa, F. Inzoli, An Integrated lumped parameter-CFD approach for off-design ejector performance evaluation, Energy Convers. Manage. 105 (2015) 697–715.

[15] S. Varga, A.C. Oliveira, B. Diaconu, Numerical assessment of steam ejector efficiencies using CFD, Int. J. Refrig. 32 (2009) 1203–1211.

[16] F. Liu, E.A. Groll, Study of ejector efficiencies in refrigeration cycles, Appl. Therm. Eng. 52 (2013) 360–370.

[17] G. Besagni, R. Mereu, E. Colombo, CFD study of ejector efficiencies, in: ASME 2014 12th Biennal Conference on Engineering Systems Design and Analysis, Vol. Dynamics, Vibration and Control; Energy; Fluid Engineering; MIcro and Nano Manufacturing, ESDA2014-20053, Copenhagen, Denmark, 2014, p. V02T11A004.

[18] L. Zheng, J. Deng, Research on CO2 ejector component efficiencies by experiment measurement and distributed-parameter modeling, Energy Convers. Manage. 142 (2017) 244–256.

[19] X. Wang, J. Yu, An investigation on the component efficiencies of a small two-phase ejector, Int. J. Refrig. 71 (2016) 26–38.

[20] G. Besagni, R. Mereu, G. Di Leo, F. Inzoli, A study of working fluids for heat driven ejector refrigeration using lumped parameter models, Int. J. Refrig. (2015) 154–171.

[21] G. Besagni, F. Inzoli, Computational fluid-dynamics modeling of supersonic ejectors: Screening of turbulence modeling approaches, Appl. Therm. Eng. 117 (2017) 122–144.

[22] S. He, Y. Li, R.Z. Wang, Progress of mathematical modeling on ejectors, Renew. Sustain. Energy Rev. 13 (2009) 1760–1780.

[23] G.E. Alves, Ejector design and performance, Fluid Particle Mech. (1951) 69–79.

[24] F. Marsano, L. Magistri, A.F. Massardo, Ejector performance influence on a solid oxide fuel cell anodic recirculation system, J. Power Sources 129 (2004) 216–228.

[25] Y. Zhu, W. Cai, C. Wen, Y. Li, Fuel ejector design and simulation model for anodic recirculation SOFC system, J. Power Sources 173 (2007) 437–449.

[26] H.K. Versteeg, W. Malalasekera, An Introduction to Computational Fluid Dynamics: The Finite Volume Method, Pearson Education, 2007.

[27] S. Croquer, S. Poncet, Z. Aidoun, Turbulence modeling of a single-phase R134a supersonic ejector, Part 1: Numerical benchmark, Int. J. Refrig. 61 (2016) 140–152.

[28] Y. Bartosiewicz, Z. Aidoun, P. Desevaux, Y. Mercadier, CFD-experiments integration in the evaluation of six turbulence models for supersonic ejectors modeling, in: Proceedings of Integrating CFD and Experiments, vol. 26, Glasgow, 2003, pp. 71–78.

[29] J. Kolář, V. Dvořák, Verification of K-ω SST turbulence model for supersonic internal flows, World Acad. Sci. Eng. Technol. 81 (2011) 262–266.

[30] J. Gagan, K. Smierciew, D. Butrymowicz, J. Karwacki, Comparative study of turbulence models in application to gas ejectors, Int. J. Therm. Sci. 78 (2014) 9–15.

[31] S.M. El-Behery, M.H. Hamed, A comparative study of turbulence models performance for separating flow in a planar asymmetric diffuser, Comput. Fluids 44 (2011) 248–257.

[32] A. Balabel, A.M. Hegab, M. Nasr, S.M. El-Behery, Assessment of turbulence modeling for gas flow in two-dimensional convergent–divergent rocket nozzle, Appl. Math. Model. 35 (2011) 3408–3422.

[33] N.J. Georgiadis, T. Chitsomboon, J. Zhu, Modification of the two-equation turbulence model in NPARC to a Chien Low Reynolds Number k-epsilon formulation, in: NASA, 1994.

[34] X. Han, P. Sagaut, D. Lucor, On sensitivity of RANS simulations to uncertain turbulent inflow conditions, Comput. Fluids 61 (2012) 2–5.

[35] B.J. Huang, J.M. Chang, C.P. Wang, V.A. Petrenko, A 1-D analysis of ejector performance, Int. J. Refrig. 22 (1999) 354–364.

[36] Y. Zhu, Y. Li, New teoretical model for convergent nozzle ejector in the proton exchange membrane fuell cell system, J. Power Sources 191 (2009) 510–519.

[37] D. Maddiotto, Analysis of the behavior of an ejector in off-design conditions, Master of Science, Politecnico di Milano, Energy Department, 2013.

[38] P. Colonna, T.P. van der Stelt, FluidProp: a program for the estimation of thermo physical properties of fluids, in: Energy Technology Section, Delft University of Technology, The Netherlands, 2004.

[39] F. Liu, Review on ejector efficiencies in various ejector systems, in: International Refrigeration and Air Conditioning Conference, Purdue, 2014.

[40] G. Grazzini, A. Mariani, A simple program to design a multi-stagejet-pump for refrigeration cycles, Energy Convers. Manage. 39 (1998) 1827–1834.

[41] N.H. Aly, A. Karameldina, M.M. Shamloul, Modelling and simulation of steam jet ejectors, Desalination 123 (1999) 1–8.

[42] D. Li, E.A. Groll, Transcritical CO2 refrigerationcycle with ejector-expansion device, Int. J. Refrig. 28 (2005) 766–773.

[43] J. Yu, Y. Li, A theoretical study of a novel regenerative ejector refrigeration cycle, Int. J. Refrig. 30 (2007) 464–470.

[44] J. Yu, H. Zhao, Y. Li, Application of an ejector in autocascade refrigeration cycle for the performance improvement, Int. J. Refrig. 31 (2008) 279–286.

[45] S. Fangtian, M. Yitai, Thermodynamic analysis of transcritical CO2 refrigeration cycle with an ejector, Appl. Therm. Eng. 31 (2011) 1184–1189.

[46] M.A.R.S. Al-Baghdadi, Modelling of proton exchange membrane fuel cell performance based on semi-empirical equations, Renew. Energy 30 (2005) 1587–1599.

[47] Y. Zhu, Y. Li, W. Cai, Numerical modeling and analysis of ejector in the proton exchange membrane fuel cell system, in: 4th IEEE Conference on Industrial Electronics and Applications, 2009 (ICIEA 2009), IEEE, 2009, pp. 2859–2861.

[48] C. Spiegel, PEM fuel cell modeling and simulation using MATLAB, Access Online via Elsevier, 2011.

[49] N. Ahmadi, H. Taraghi, M. Sadeghiazad, A numerical study of a three-dimensional proton exchange membrane fuel cell (Pemfc) with parallel and counter flow gas channels, Iranian J. Sci. Technol. Trans. Mech. Eng. 39 (2015) 309–323.

[50] N. Ahmadi, A. Dadvand, S. Rezazadeh, I. Mirzaee, Analysis of the operating pressure and GDL geometrical configuration effect on PEM fuel cell performance, J. Brazilian Soc. Mech. Sci. Eng. 38 (2016) 2311–2325.

[51] A.P. Manso, F.F. Marzo, J. Barranco, X. Garikano, M. Garmendia, Mujika, Influence of geometric parameters of the flow fields on the performance of a PEM fuel cell: a review, Int. J. Hydrogen Energy 37 (2012) 15256–15287.

[52] R.F. Mann, J.C. Amphlett, M.A. Hooper, H.M. Jensen, B.A. Peppley, P.R. Roberge, Development and application of a generalised steady-state electrochemical model for a PEM fuel cell, J. Power Sources 86 (2000) 173–180.

[53] R. Cownden, M. Nahon, M.A. Rosen, Exergy analysis of a fuel cell power system for transportation applications, Exergy, Int. J. 1 (2001) 112–121.

[54] J.C. Amphlett, R. Baumert, R.F. Mann, B.A. Peppley, P.R. Roberge, T.J. Harris, Performance modeling of the Ballard Mark IV solid polymer electrolyte fuel cell I. Mechanistic model development, J. Electrochem. Soc. 142 (1995) 1–8.

[55] F. Laurencelle, R. Chahine, J. Hamelin, K. Agbossou, M. Fournier, T. Bose, A. Laperriere, Characterization of a Ballard MK5-E proton exchange membrane fuel cell stack, Fuel Cells 1 (2001) 66–71.

[56] M. Dadvar, E. Afshari, Analysis of design parameters in anodic recirculation system based on ejector technology for PEM fuel cells: a new approach in designing, Int. J. Hydrogen Energy 39 (2014) 12061–12073.

[57] D.-W. Sun, Experimental investigation of the performance characteristics of a steam jet refrigeration system, Energy Sources 19 (1997) 349–367.